NAVAL POSTGRADUATE SCHOOL

MONTEREY, CALIFORNIA

THESIS

STUDIES OF RAMAN, RAMSEY, AND SPIN ECHO SPECTROSCOPIES USING COUNTER-PROPAGATING FIELDS FOR USE IN ATOM INTERFEROMETERS

by

Anthony F. Burns

September 2023

Thesis Advisor:	Frank A. Narducci
Second Reader:	Fabio Durante Pereira Alves

THIS PAGE INTENTIONALLY LEFT BLANK

REPORT DOCUMENTATION PAGE	*Form Approved OMB No. 0704-0188*

1. AGENCY USE ONLY ***(Leave blank)***	**2. REPORT DATE** September 2023	**3. REPORT TYPE AND DATES COVERED** Master’s thesis

4. TITLE AND SUBTITLE STUDIES OF RAMAN, RAMSEY, AND SPIN ECHO SPECTROSCOPIES USING COUNTER-PROPAGATING FIELDS FOR USE IN ATOM INTERFEROMETERS	**5. FUNDING NUMBERS**
6. AUTHOR(S) Anthony F. Burns	
7. PERFORMING ORGANIZATION NAME(S) AND ADDRESS(ES) Naval Postgraduate School Monterey, CA 93943-5000	**8. PERFORMING ORGANIZATION REPORT NUMBER**
9. SPONSORING / MONITORING AGENCY NAME(S) AND ADDRESS(ES) N/A	**10. SPONSORING / MONITORING AGENCY REPORT NUMBER**

11. SUPPLEMENTARY NOTES The views expressed in this thesis are those of the author and do not reflect the official policy or position of the Department of Defense or the U.S. Government.

12a. DISTRIBUTION / AVAILABILITY STATEMENT Approved for public release. Distribution is unlimited.	**12b. DISTRIBUTION CODE** A

13. ABSTRACT (maximum 200 words)

The Department of Defense relies on many platforms that require inertial sensors to operate in Global Positioning System (GPS)–compromised environments to provide or verify navigational data. The current generation of sensors in use are subject to sensitivity limitations and drift errors that can compound significantly over time in GPS-contested areas. Inertial sensors based on atom interferometers could provide navigational data that is significantly more accurate and less prone to drift (and therefore navigational errors). This research builds upon previous work (Manicchia in 2020, Gervis in 2021) in which an atomic interferometer was constructed and studied. In this thesis, I demonstrate a path toward making inertially sensitive measurements with this apparatus. In contrast to the previous work, I use counter-propagating Raman fields that can achieve inertial sensitivity. However, these Raman fields are sensitive to non-trivial transverse velocities of our atom beam. I demonstrate a method to reduce these transverse velocities using an optical molasses, but do not pursue this in the apparatus due to spatial considerations. I explore the difference between Ramsey and spin echo spectroscopies, forms of atomic interference, in co- and counter-propagating configurations, the second of which is inertially sensitive. I also demonstrate that interference is still visible in the counter-propagating geometry, laying the foundation for a fully inertially sensitive interferometer.

14. SUBJECT TERMS laser, quantum gyroscope, atom interferometer, accelerometer, saturated absorption, laser cooling	**15. NUMBER OF PAGES** 93
	16. PRICE CODE

17. SECURITY CLASSIFICATION OF REPORT Unclassified	**18. SECURITY CLASSIFICATION OF THIS PAGE** Unclassified	**19. SECURITY CLASSIFICATION OF ABSTRACT** Unclassified	**20. LIMITATION OF ABSTRACT** UU

NSN 7540-01-280-5500

Standard Form 298 (Rev. 2-89)
Prescribed by ANSI Std. 239-18

THIS PAGE INTENTIONALLY LEFT BLANK

STUDIES OF RAMAN, RAMSEY, AND SPIN ECHO SPECTROSCOPIES USING COUNTER-PROPAGATING FIELDS FOR USE IN ATOM INTERFEROMETERS

Anthony F. Burns
Captain, United States Marine Corps
BS, United States Naval Academy, 2017

Submitted in partial fulfillment of the
requirements for the degree of

MASTER OF SCIENCE IN APPLIED PHYSICS

from the

NAVAL POSTGRADUATE SCHOOL
September 2023

Approved by: Frank A. Narducci
Advisor

Fabio Durante Pereira Alves
Second Reader

Frank A. Narducci
Chair, Department of Physics

THIS PAGE INTENTIONALLY LEFT BLANK

ABSTRACT

The Department of Defense relies on many platforms that require inertial sensors to operate in Global Positioning System (GPS)–compromised environments to provide or verify navigational data. The current generation of sensors in use are subject to sensitivity limitations and drift errors that can compound significantly over time in GPS-contested areas. Inertial sensors based on atom interferometers could provide navigational data that is significantly more accurate and less prone to drift (and therefore navigational errors). This research builds upon previous work (Manicchia in 2020, Gervis in 2021) in which an atomic interferometer was constructed and studied. In this thesis, I demonstrate a path toward making inertially sensitive measurements with this apparatus. In contrast to the previous work, I use counter-propagating Raman fields that can achieve inertial sensitivity. However, these Raman fields are sensitive to non-trivial transverse velocities of our atom beam. I demonstrate a method to reduce these transverse velocities using an optical molasses, but do not pursue this in the apparatus due to spatial considerations. I explore the difference between Ramsey and spin echo spectroscopies, forms of atomic interference, in co- and counter-propagating configurations, the second of which is inertially sensitive. I also demonstrate that interference is still visible in the counter-propagating geometry, laying the foundation for a fully inertially sensitive interferometer.

THIS PAGE INTENTIONALLY LEFT BLANK

Table of Contents

1 Introduction **1**
1.1 Project Motivation 1
1.2 Project Background 2

2 Theory **5**
2.1 Interferometry 5
2.2 Phase Shifts 7
2.3 The Raman Process 11
2.4 AC Stark and Zeeman Shifts 12
2.5 Cooling and Trapping of Atoms 14
2.6 Repumping. 16
2.7 Detection 19
2.8 Optical Pumping 19
2.9 Simulations 20

3 Experimental Setup **27**
3.1 Apparatus Design 27
3.2 Saturated Absorption 29
3.3 Experimental Parameters 31
3.4 Lock-in Detection 39
3.5 Transverse Cooling 40
3.6 Raman Setup 41
3.7 Rabi Oscillations 44
3.8 AC stark and Zeeman shifts 44
3.9 Interferometer 46

4 Results **49**
4.1 Optical Molasses 49
4.2 Raman Spectroscopy 52

4.3 Co- and Counter-Propagating Ramsey Interference 58
4.4 Scan Time 60
4.5 Spin Echo Interference 63

5 Conclusions **67**

List of References **69**

Initial Distribution List **75**

List of Figures

Figure 2.1 Interferometer 6

Figure 2.2 Energy Diagram for two-level atom 14

Figure 2.3 Infrared photo of 2D MOT 16

Figure 2.4 Rubidium line data 18

Figure 2.5 Effects on Rabi oscillations from velocity averaging and atom beam divergence 21

Figure 2.6 Ramsey spectrum without and with velocity averaging 22

Figure 2.7 Max contrast vs. slit spacing 23

Figure 2.8 Effects on counter-propagating Ramsey from velocity averaging and atom beam divergence 24

Figure 2.9 Spin Echo Slit Spacing 25

Figure 3.1 Cooling arm 28

Figure 3.2 Vacuum chamber setup 29

Figure 3.3 Saturated absorption setup 30

Figure 3.4 Cooling transition saturated absorption spectrum 31

Figure 3.5 Scan of detection peak and cooling transition 33

Figure 3.6 Velocity spread of the atoms 36

Figure 3.7 Most probable velocity results 37

Figure 3.8 Gaussian fit for 20ms pulse width 38

Figure 3.9 Gaussian fit for 2ms pulse width 39

Figure 3.10 Optical molasses setup 41

Figure 3.11 Raman setup and optical paths. 42

Figure 3.12 Raman fields profile 43
Figure 3.13 Zeeman shift vs. coil current 45
Figure 3.14 Interferometer setup 47
Figure 3.15 Mask 48

Figure 4.1 Cooling power versus waveplate setting 50
Figure 4.2 Transverse cooling over polarizations 51
Figure 4.3 Linewidth and Peak amplitude versus polarization setting 52
Figure 4.4 Full Raman spectrum 54
Figure 4.5 Raman co- to counter-propagating progression 55
Figure 4.6 Co-propagating Rabi oscillation 56
Figure 4.7 Raman linewidth 57
Figure 4.8 Ramsey co- to counter-propagating progression 58
Figure 4.9 Counter-propagating Rabi 59
Figure 4.10 Ramsey Interference 60
Figure 4.11 Ramsey contrast values 61
Figure 4.12 Center peak contrast fits 62
Figure 4.13 Modified Gaussian fit to Ramsey 63
Figure 4.14 Spin echo co- to counter-propagating progression 64
Figure 4.15 Spin echo interference 65

List of Tables

Table 3.1 Getter current SNR ratios 34

THIS PAGE INTENTIONALLY LEFT BLANK

List of Acronyms and Abbreviations

AOM	acousto-optic modulator
GPS	Global Positioning System
HWHM	half width at half maximum
INS	inertial navigation systems
MOT	magneto-optical trap
PBS	polarizing beam splitter
PMT	photomultiplier tube
RF	radio frequency
SNR	signal to noise ratio

THIS PAGE INTENTIONALLY LEFT BLANK

Acknowledgments

I would like to thank Dr. Narducci for the countless hours he spent teaching, coaching, and guiding me throughout this process, time that I stole from his other pursuits, projects, and his family. He exemplified a constant pursuit of excellence that I strove to match. I would like to thank Dr. Jeff Lee for putting up with a daily barrage of questions and showing me how to turn on the system an embarrassing amount of times. I would also like to extend my sincerest gratitude to Jeffrey Catterlin for printing some critical parts in the waning days of the experiment. I would lastly like to thank my family, friends, and colleagues for their love and support as well as inspiration and perspective during this process.

THIS PAGE INTENTIONALLY LEFT BLANK

CHAPTER 1:
Introduction

1.1 Project Motivation

The ability to effectively navigate is a critical task—if not the most critical task—that the Navy executes on a day-to-day basis in support of its various missions around the globe. Over the centuries, many different methods to navigate have been employed ranging from celestial navigation (still taught at the Naval Academy) to more modern charts and maneuver boards to radio navigation and inertial navigation [1], [2]. However, with the arrival of the first satellite navigation system, Transit in 1964, the U.S. Navy ushered in a new era of navigation [3]. Currently, there are several global navigation satellite systems in use around the world. The U.S. uses the Global Positioning System (GPS) with users—including the U.S. military—becoming ever more reliant on it [2], [4].

This over-reliance on GPS is a serious vulnerability which the military has been aware of for well over a decade [5]. GPS systems are capable of being interfered with and manipulated in several different ways by bad actors as well as Nature. One way the GPS can be compromised is through signal interference or jamming which occurs when GPS signals are blocked or disrupted, resulting in inaccurate or unreliable location data [6]. Spoofing is another method to compromise GPS, in which adversaries can create false GPS signals to deceive users or manipulate navigation systems due to unencrypted or weakly encrypted GPS signals using commercial off-the-shelf technology [6]–[8]. America's competitors have developed or are developing these capabilities [9]. Nature can also degrade GPS effectiveness through solar weather and other adverse atmospheric conditions [9], [10]. While the U.S. can and should improve and harden its GPS technology, it needs to reduce its dependence on it and explore other solutions and alternatives for navigation.

One solution to this vulnerability is to develop more robust inertial navigation systems (INS). The basic technology has been around since the first half of the 20th century, but has traditionally been expensive and unreliable over long time scales [2]. Inertial navigation is a method that, to quote Charles Stark Draper, an American pioneer in inertial navigation, "does for geometry. . . what a watch does for time" [2]. INS use measurements of acceleration and rotation and integrates them to determine velocity and distance. These signal are combined with an initial location and velocity to provide accurate location data. The calculations can be repeated using updated acceleration and rotation data to provide subsequent position information for a moving platform. These equations have been around since Newton, but the ability to accurately navigate from inertial measurements is a development of the 20th century.

Two current sensors that the U.S. military uses to measure rotation are the ring laser gyroscope and fiber optical gyroscope which measure rotation [11], [12]. The outputs of these sensors are integrated over time by a computer to provide the necessary navigational data. A similar process is used for acceleration data. An important note on this process is that due to the integration process any errors in measurements will compound overtime. Another issue is the fluctuations in the gyroscope bias, commonly referred to as drift. The drift rate is a key measure of performance for accelerometers and gyroscopes. The current generation of accelerometers used today have drift rates around 1 nautical mile over a 24-hour period, with state of the art ones up to 360 hours [2], [13]–[15]. The work presented in this thesis lays the foundation for reducing drift rates. These sensors also have precision limits based on how sensitive they are. This sensitivity limit is the second problem I will address.

I will attempt to address the previously stated problems and improve upon previous sensors by developing an atom interferometer accelerometer/gyroscope. The design of the apparatus is based on previous research which has shown the potential for significantly decreasing drift rates and increasing sensitivity of the sensor [16], [17]. Successful execution of this work will provide a promising development for improving the Department of Defense's navigational capabilities in GPS compromised environments.

1.2 Project Background

Atom interferometers were first developed in the early 1990's, and have been used to measure physical quantities such as acceleration, rotation, gravity, and electromagnetic fields [18]–[21]. More recently, they have been used for several different applications, with their use in inertial sensors being most relevant to my research [22]–[24].

Atom interferometers work by exploiting the quantum mechanical properties of matter to conduct extremely precise measurements. The main element of an atom interferometer is a collection of cold atoms traveling along a trajectory. The atoms are subject to an "atom beam splitter" (usually comprised of laser beams) that splits the trajectory into two separate paths which move away from each other. The beam splitter creates a quantum superposition of states, where the atoms simultaneously take both paths. Then the atoms are redirected towards each other, the paths recombine after a certain time, and an interference pattern is detected by analyzing the resulting phase difference between the two paths. The interference occurs due to the quantum mechanical nature of the atoms, with their wave-like properties leading to constructive or destructive interference depending on the relative phases acquired during their evolution along each path.

The use of atom interferometers has several advantages over other measurement devices and techniques. Firstly, they are incredibly sensitive, capable of detecting extremely small changes in the physical quantities being measured. As an example, the sensitivity of an atom interferometer gyroscope is proportional to the mass, m, of the atom as shown in Equation 1.1 [25],

$$\Omega_{min} = \frac{\hbar \Delta\phi_{min}}{2mA}. \tag{1.1}$$

where in this example, Ω_{min} is the minimum detectable rotation based on the minimum measurable phase shift, $\Delta\phi_{min}$, that we can measure (and so smaller is better), $\hbar$ is the reduced Plank's constant, and A is the area enclosed by the atom interferometer. We can see that the minimum measurable rotation is inversely proportional to the mass of the atoms, so that heavier atoms lead to smaller detectable rotation. When compared with the weight of photons, using atoms can theoretically produce as much as 10 orders of magnitude increase in sensitivity [16]. We get an effective mass of a photon by equating $E = mc^2 = \hbar\omega$ and using optical frequencies. Even when accounting for limitations that result from using atoms e.g. much smaller atom flux, inability to recirculate atoms in a resonator etc., the realistic increase is around three to four orders of magnitude [26]. Additionally, due to the quantum nature of the measurements, the data produced is extremely precise with very small uncertainties. The combination of these traits make atom interferometers ideal for use by the military in navigation via inertial sensors.

Another key trait of atom interferometers is that they are sensitive to both acceleration and rotation. However, the determination whether a measurement is acceleration or rotation can only be achieved with two interferometers (as described later in Section 2.2). This has been achieved by previous research [27], [28] that used balls of atoms collected in a 3D magneto-optical trap (MOT) fed by a 2D MOT (see Section 2.5 for more on MOTs). However, this type of system is complicated, requires significant power and precise timing, and has several challenging effects such as dead time effects. Therefore, a motivation for my project is to eliminate the use of 3D MOTs and work with continuous beams.

This thesis builds upon previous research that designed, built, and characterized the main components of a continuous beam atom interferometer by working towards being able to make inertially sensitive measurements of the Earth's rotation [16]. This interferometer uses the 85 nucleon isotope of the Rubidium atom (^{85}Rb). This atom is chosen based on its well-characterized energy levels as well as the fact that the main atomic transition used in these type of experiments is well matched to the operating frequency of many inexpensive and commonly available lasers [16]. Also, as discovered in previous research from this lab, producing the required frequency difference in laser fields to drive the resonance used in the atom optics is very convenient to do using standard radio frequency (RF) components and an off-the-shelf acousto-optic modulator (AOM). This convenience is a result of the ground state splitting being smaller in ^{85}Rb (3.0 GHz) than in ^{87}Rb (6.8 GHz). My work explored transverse cooling, reducing the velocity and spacial spread of the atoms, as well as inertially sensitive configurations of the interferometer. Chapter 2 of this thesis covers the theory of the interaction of a two-level atom with a single-mode laser field and how the interaction can be used to laser-cool neutral atoms and also used to build atom interferometers. I discuss the need for a repumping laser and an optical pump laser. In this chapter, I also discuss the co-propagating (inertially insensitive) and counter-propagating (inertially sensitive) configuration of the Raman process as well as Ramsey and spin echo interference. In Chapter 3, I cover the experimental setup including the how we prepare the lasers, how we create a Raman process, and the individual optical paths and methods used in the interferometer. In Chapter 4, I present the experimental results and compare them with theory. Finally, in Chapter 5, I present my conclusions, outlook, and future work.

CHAPTER 2:
Theory

In this chapter, I lay out much of the scientific theory that serves as the foundation for my experiment. I cover the key topics of atomic interferometry, cooling and trapping, repumping and optically pumping, and detection. Simulations of the interference effects are also be presented. Much of this work builds on, or is adapted from, Michael Manicchia's 2020 Naval Postgraduate School dissertation [16]. I have attempted to remain consistent in the coloring of the lasers in diagrams with red belonging somewhat counterintuitively to the cooling transition and blue belonging to the repump transition, both of which will be discussed in this section.

2.1 Interferometry

My experiments use atom interferometers which are very similar in wave physics to optical interferometers, which have been in existence for significantly longer. These optical interferometers use light waves or photons from a single source and split their trajectories into two different paths before recombining them to observe interference between the two paths. One example is a Mach-Zehnder interferometer which is analogous to the atom interferometer I use. This type of interferometer is comprised of a single light source which emits waves which are split by a beam splitter and sent down two different paths. The paths are then redirected towards each other by mirrors, and recombined by a second beam splitter allowing any difference in the phase accumulated in each arm to be observed through the process of constructive and destructive interference. My version of this set up uses atom matterwaves instead of light waves and uses light pulses instead of mirrors. Figure 2.1 depicts the spatial process of the interferometer.

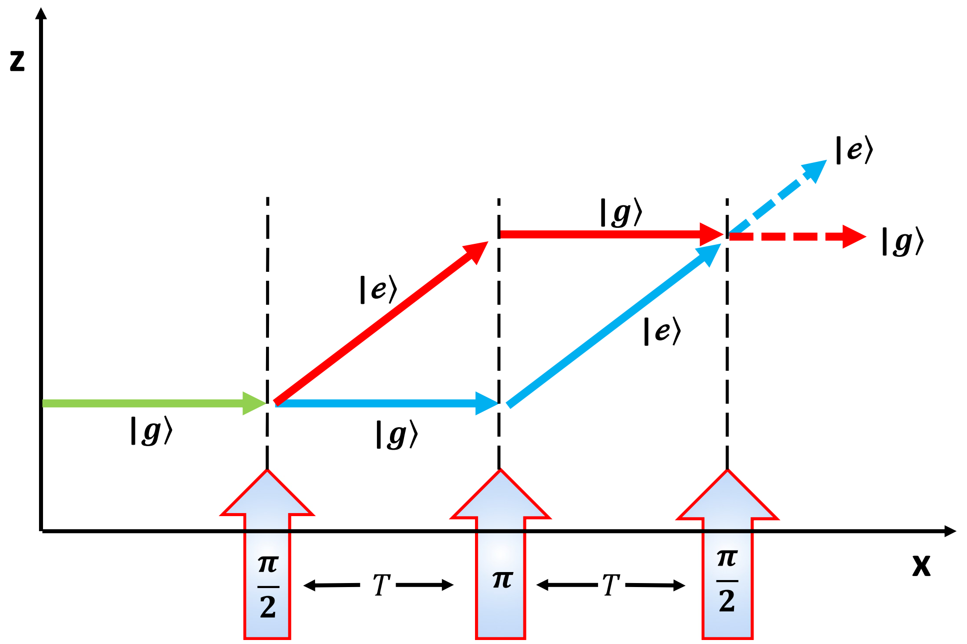

Figure 2.1. Graphical representation of my interferometer depicting the two paths on which the atoms propagate and the laser pulses that serve as atom mirrors (π- pulse) and atom beam splitters ($\pi/2$- pulse).

This process starts by sending cooled atoms in their ground state, $|g\rangle$, along the x-axis of my experiment. In this context, *cooled* refers to a lower velocity *spread* than for a room temperature gas. As discussed later in this thesis (Section 2.5), the atoms, which have been cooled, emanate from a 2D MOT. The atoms then encounter a light pulse of finite length, referred to as $\pi/2-$ pulse, that sends the atoms into a superposition of ground and excited states, $|g\rangle$ and $|e\rangle$, and provides a momentum kick to the excited state. This momentum kick is $p = \hbar k$, where k is the laser wavenumber aligned away from the direction of the laser providing the pulse, and $\hbar$ is the reduced Plank constant. A small distance (several millimeters in my experiment) after the first light pulse, the atoms encounter a light pulse referred to as a $\pi-$ pulse which serves to flip the states of the atoms. The atoms that were in the ground state are now in the excited state and they have received a momentum kick as previously described. The atoms initially in the excited state before the pulse are now in the ground state. They receive a momentum kick opposite to the direction of laser propagation as a result from the process causing the stimulated emission of a photon. After a second small distance nominally symmetric to the distance between the first and second light pulses, the atoms are recombined by a second $\pi/2-$ pulse and the energy states of the atoms are measured. In my experiment, I measure the number of atoms in the excited state which will depend on the difference in length of the two paths as a result of the interference process. The time between pulses (referred to as free evolution T) is critical to my calculations as the probability of finding atoms in the excited state is interferometrically sensitive to T. Furthermore, the interferometer encloses physical space, which allows for inertial sensitivity [29].

2.2 Phase Shifts

The previous section highlights how differences in the phase acquired by the atoms in the two arms of the interferometer interferometrically impact the number of atoms in the excited state at the output of the interferometer (which is the parameter I measure in my experiments) [25], [27]. The phase shift I am looking for is a result of inertial changes, i.e., a rotation or an acceleration and not resulting from motion along the classical path of the atoms [29]. An acceleration would produce the following phase shift

$$\Delta\phi_{acc} = \vec{k}_{eff} \cdot \vec{\alpha} T^2, \tag{2.1}$$

where $\Delta\phi_{acc}$ is the change in phase due to acceleration, $\vec{k}_{eff}$ is the effective wave vector defined in Section 2.3.1, $\vec{\alpha}$ is the acceleration vector, and T is the free evolution time between light pulses in the interferometer. A rotation phase shift is characterized by

$$\Delta\phi_{rot} = \frac{2m}{\hbar}\vec{\Omega} \cdot \vec{A}, \tag{2.2}$$

where $\vec{\Omega}$ is the rotation vector, m is the mass of the atom (or photon for optical interferometers) and $\vec{A}$ is the area vector of the interferometer whose magnitude is the area enclosed by the atoms and whose direction is given by the cross product of the original velocity vector with the k vector of the laser. The total phase shift for one interferometer is calculated by adding these two phase shifts together.

However, with just one interferometer it is not possible to determine if a phase shift is caused by acceleration or rotation. By adding a second atom interferometer to the set up with the atoms of the second interferometer oriented in the opposite direction to the atoms of the first interferometer, the sign of the phase shift can change. The sign of $\vec{A}$ changes (often referred to in the literature as “flipping the Sagnac loop”) and therefore the sign of $\Delta\phi_{rot}$ flips. If the phase shifts of the two interferometers are added together, the phase shifts caused by rotation would cancel leaving only the phase shift caused by acceleration, with the contribution doubled. It then follows that by subtracting the two total phase shifts, the phase shifts caused by acceleration will cancel leaving only the phase shift cause by rotation, with the contribution again doubled. The eventual long-term goal of my overall project is the implementation of the simultaneous interferometers. Although I did not attain this goal within this thesis project, it was important to understand the underlying theory and motivation to properly frame my research.

2.2.1 Rabi Oscillations

As discussed in the previous section, the fundamental building blocks of an atom interferometer are the light pulses from the atom optics. A critical step in creating these light pulses is the interaction of a laser field with a two-level atom. This problem is by now a textbook problem [30]–[32] where it is shown that the atom undergoes *Rabi oscillations*. In this section, I briefly outline the salient points but the reader is referred to the literature for details [30]–[32].

When an atom is illuminated by a single mode laser field whose frequency is tuned close to the atomic transition frequency, the atomic population begins to oscillate (see Figure 2.2 for a representation of a two-level atom). These oscillations between the ground and excited states are characterized by a frequency, called the Rabi frequency, which is typically denoted by Ω (Not to be confused with $\vec{\Omega}$ which is the rotation rate of a platform that was discussed in an earlier section). Despite being illuminated by a strongly-coupled, near-resonance laser, an atom can still decay by spontaneous emission back to the ground state before being promoted again to the excited state. When the atom is undergoing Rabi oscillations, the population oscillates from fully in $|g\rangle$, through an even superposition in both $|g\rangle$ and $|e\rangle$, to fully in $|e\rangle$. This oscillation frequency is a function of the laser field amplitude, the detuning of the laser from atomic resonance, the polarization vector of the laser and the dipole moment of the atom. When the system is left on for a length of time determined by these parameters such that the product of the Rabi frequency times time is equal to $\pi/2$, then we say a $\pi/2$- pulse has occurred, and the system is the equal superposition state $|\psi\rangle = \frac{1}{\sqrt{2}}(|g\rangle + |e\rangle)$. Similarly, a π- pulse occurs when the laser is left on for a time T_{pulse} such that $\Omega T_{pulse} = \pi$ and all the atoms in the ground state move to the excited state (and equivalently, all the atoms in the excited state move to the ground state). These pulses are produced through careful management of the laser's detuning, the amount of time the atoms spend illuminated, and the power of the laser. These pulses can be configured in different way to produce different types of atom interferometers, as I will now discuss in the next section.

2.2.2 Ramsey and Spin Echo Interference

A standard interferometry scheme was first introduced by Norman Ramsey which involves a $\pi/2 - \pi/2$ pulse sequence with a free evolution time T in between the pulses [33]. The state of the system evolves as follows:

$$|\psi(t = 0)\rangle = |g\rangle \tag{2.3}$$

where the wave functions of the atoms start in the ground state and are allowed to evolve in a $\pi/2$ pulse of light.

$$|\psi(t = \tfrac{\pi}{2\Omega})\rangle = \frac{1}{\sqrt{2}}|g\rangle + \frac{i}{\sqrt{2}}|e\rangle, \tag{2.4}$$

where Ω is the intensity of the laser. The atoms are then allowed to progress in the dark during free evolution time (T),

$$|\psi(t = \tfrac{\pi}{2\Omega} + T)\rangle = \frac{1}{\sqrt{2}}|g\rangle + e^{i\delta T/2}\frac{i}{\sqrt{2}}|e\rangle, \tag{2.5}$$

where δ is the laser detuning, before encountering the second $\pi/2$ pulse

$$|\psi(t = 2\tfrac{\pi}{2\Omega} + T)\rangle = \frac{1}{\sqrt{2}}\left(\frac{1}{\sqrt{2}}|g\rangle + \frac{i}{\sqrt{2}}|e\rangle\right) + \frac{i}{\sqrt{2}}e^{i\delta T/2}\left(\frac{i}{\sqrt{2}}|g\rangle + \frac{1}{\sqrt{2}}|e\rangle\right). \tag{2.6}$$

the projection of the excited state onto the current wavefunction is now calculated,

$$\langle e|\psi\rangle = \frac{i}{\sqrt{2}} e^{i\delta T_m/2} + \frac{i}{\sqrt{2}} e^{i\delta T/2} e^{i\delta T_m/2} \tag{2.7}$$

where T_m is the free evolution time before the measurement. I then take the modulus squared to find the probability of finding an atom in the excited state

$$|\langle e|\psi\rangle|^2 = \frac{1}{4} \left|1 + e^{i\delta T/2}\right|^2 \tag{2.8}$$

I performed the same equation for the spin echo configuration and my result was

$$|\langle e|\psi\rangle|^2 = \frac{1}{2} \left|1 + e^{i\delta T/2}\right|^2 . \tag{2.9}$$

I use experimentally measured Rabi oscillations to determine proper power levels and single-photon detuning.

Another combination of pulses is the $\pi/2 - \pi - \pi/2$ pulse sequence, often called the *spin echo* pulse sequence. As the name implies, the sequence consists of a $\pi/2$- pulse, a free-evolution time T_1, a π- pulse, a free evolution time T_2 and a final $\pi/2$- pulse. Repeating the same type of state calculations shown in the preceding paragraph, I find that the probability of finding the atom in the excited state at the output of the interferometer is given by

$$|\langle e|\psi\rangle|^2 = \frac{1}{2} \left(1 - \cos \frac{\delta(T_1 - T_2)}{2}\right) . \tag{2.10}$$

The original motivation for studying spin echo versus Ramsey is not relevant to my work other than to note that this is exactly the pulse sequence depicted in Figure 2.1.

The entire discussion in this section assumes that the pulses of light applied to the atoms are perfect π and $\pi/2$- pulses. For many types of atomic systems, this can be a good assumption. However, as I discuss in the experimental section 3.3.2), my pulses are based on the transit time of atoms through a continuous laser beam of some spatial extent. Because the atoms have a spread in their velocity (both in speed and direction), there is a only one velocity group that has perfect pulses—all others have imperfect pulses. I ran simulations to understand the impact of averaging over these variables in the different experimental configurations.

The results of those simulations are discussed in Section 2.9.

2.3 The Raman Process

There are a few different ways to create the $\pi/2 - \pi - \pi/2$ light pulses used in the interferometer. One method is to use three different laser beams, which was previously tried in my lab. However, it was found that the strong Gaussian profile of the fields caused interference to disappear [16]. A second way is to pass the atoms though a micro-fabricated grating. The grating causes diffraction of the atoms, much in the way an optical grating causes light diffraction. However, this has the major disadvantage of the grating needing to be installed inside the vacuum system and at the same time is not reconfigurable [18]. I chose to use a Raman process to serve as the light pulses. The process I use is a “stimulated” Raman process because a laser is used to coherently move atomic population between two different ground states ($F = 2$ and $F = 3$) without any spontaneous emission from moving into an excited state (F') (see Section 2.6 and Figure 2.4 for a detailed description of the ^{85}Rb energy levels). In order to accomplish this, I tune one laser far off-resonance with the $F = 2$ to any F' transition. I do the same with a second laser and the $F = 3$ transition. I then detune both of these laser fields by the same amount, so they are not on resonance with any individual transitions. The mismatch between the laser frequency and the atomic transition is known as single-photon detuning (δ_1 and δ_2) which I take to be nearly equal ($\delta 1 \approx \delta_2$). With this setup, it now takes two photons to go from $F = 2$ to $F = 3$, one to excite the atom to a virtual excited state and one to stimulate decay into the second ground state. The system is now in two-photon resonance. I denote the frequency difference between $F = 2$ and $F = 3$ (also known as the ground state hyperfine splitting) by Δ. I now choose the detuning of the two lasers such that $\delta_1 - \delta_2 - \Delta \approx 0$ which I say is nearly in two photon resonance. This allows for the atoms to move between the two energy levels as if in a two-level system where $F = 2$ and $F = 3$ are respectively the $|g\rangle$ and $|e\rangle$ states. The excited state F' is now simply a virtual state where the atoms do not spend any time as they cycle between ground states.

2.3.1 Co-propagating and Counter-propagating Beams

To construct an atom interferometer requires that a lot of things work together in a complex system. Fortunately, there are two configurations I can use as building blocks. The two configurations involve the two Raman beams in either a co-propagating or counter-propagating configuration. The first configuration is denoted as the co-propagating configuration and it consists of a single physical Raman fields field composed of two different frequencies (with different polarizations) propagating together directly through the vacuum chamber before being stopped by a window capon the far side of the vacuum chamber. This configuration has the advantage of allowing me to test the system, including the important features of the Raman fields (e.g. coherence, polarization, alignment) without needing some of the more difficult alignments required in the second configuration. This first configuration is, however, not inertially sensitive (thus the more difficult alignments are not necessary).

The second configuration involves counter-propagating Raman frequencies which are derived by allowing the co-propagating fields to pass fully through the vacuum chamber and reflect back on themselves by a mirror so that there are now two sets of identical beams covering the same spatial area running counter to each other. However, this configuration would drive multiple Raman resonances. In addition to two co-propagating configurations (one from each side), there would be two combinations of counter-propagating fields that would drive two Raman resonances (assuming the field had the right polarization). To greatly simplify the analysis, I used the techniques described in the next chapter to eliminate the co-propagating contributions as well as one counter-propagating contribution so that the result is only one Raman transition is driven in a counter-propagating configuration. The difference between these two configurations lies in the momentum kick the atoms receive from the laser as discussed in Section 2.1. The momentum kick was defined as $p = \hbar k$, but the wavevector, k, is more accurately k_{eff}, where $k_{eff} \equiv |k_2 - k_1| \approx 0$ for the co-propagating case and $k_{eff} \equiv k_2 - k_1 \approx 2k$ for the counter-propagating case when $k_1 \approx k_2$. Equation 2.1 contains the k_{eff} term and thus requires the counter-propagating setup for acceleration measurements. Shifts in k_{eff} also allow the interferometer to be sensitive to angular shifts and velocity averaging (presence of velocity difference between atoms) from the atoms which needs to be accounted for. Due to these considerations, Raman spectra in the co-propagating case are much easier to produce, and can be used to zero out frequency shifts in the Raman spectrum that are discussed in the next section.

2.4 AC Stark and Zeeman Shifts

I have been referring to the processes that split and redirect atoms in the interferometer in my experiment as “light pulses”, but I do not use pulsed light. Previous works from other groups have developed pulsed light interferometers from 3-dimensional traps. However, those systems involve complicated and power-intensive traps as well as complicated timing sequences as the atoms from the traps are “tossed” towards each other and pass through the interferometry region. I follow a different approach with the intent to make the overall system less complicated. Instead of using pulses to create π and $\pi/2-$ pulses, I extracted atoms from a 2-dimensional trap in the form of a continuous atomic beam and used continuous beams of light that the atoms pass through to provide the time and laser power necessary for the required changes in state. The continuous beams of light are created from one laser that passes through a mask with slits of varying configurations, see Section 3.6 for more details.

However, when using the Raman spectrum as the basis for the light pulses certain shifts need to be taken into account. These shifts are the result of unwanted effects that cause perturbations to the energy levels which can result in the peaks shifting when probed with different power levels or reshaping and spreading apart due to magnetic fields. One of the shifts results from an improper power ratio between the two frequencies that make up the Raman fields. Energy levels shift are a result of the presence of a driver laser field. Because the Raman process involves two laser fields driving two transitions, it is possible that the level shifts due to power imbalances do not exactly cancel, causing an apparent shift in the resonance frequency in the Raman spectrum (Strictly speaking it is the imbalance in the product of the transition dipole moment and laser field amplitude which is proportional to the square root of the laser power that causes the shift). This effect is known as the differential AC Stark shift and causes the Raman peaks to shift their frequencies as the laser is scanned from low to high power, as I do when performing the Rabi oscillation measurements. The second shift is when the Raman peaks widen and spread apart due to the prevailing magnetic field around the experiment from the earth. The fine-structure energy levels within the atom are actually degenerate and consist of magnetically sensitive sublevels (referred to as Zeeman levels). These levels shift proportionally to a magnetic field (for low magnetic field levels), causing the Raman spectrum to broaden and eventually separate into distinct peaks. Both of these shifts can lead to imprecision in measurements and inaccurate data. In Chapter 3, I cover how I eliminated them from the experiments.

2.5 Cooling and Trapping of Atoms

This section relies heavily on the PHD dissertation of Michael Manicchia [16], which is published online at: https://hdl.handle.net/10945/65398.

The primary ingredient of this experiment is a continuous supply of cold ^{85}Rb atoms. While other experiments in other fields that require low temperature samples use methods such as liquid nitrogen to cool atoms, my experiments use lasers to cool the atoms [34]. These cold atoms are created in a region of the apparatus referred to as the MOT, which is a term that is also applied to the group of trapped atoms themselves. The process of laser cooling is described in this section.

Consider a simplified two-energy-level atom as shown in Figure 2.2 consisting of a ground state and an excited state ($|g\rangle$ and $|e\rangle$) with energy difference ΔE. The difference in energy can be written in terms of frequency as $\Delta E = hf$ or $\Delta E = \hbar\omega_o$ which I get from the Plank-Einstein relation, where ω_o is the resonant atomic frequency associated with the transition between these two states.

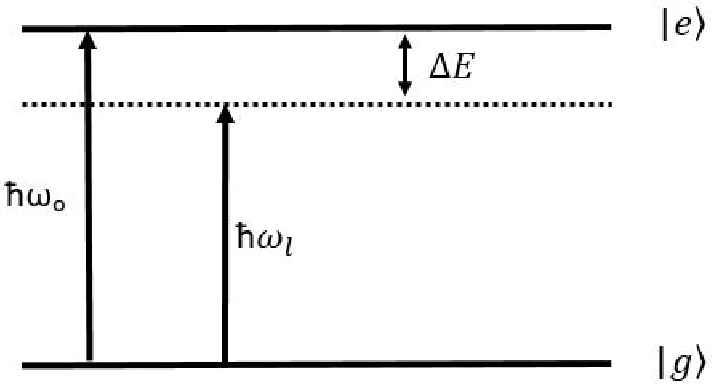

Figure 2.2. Diagram of a two-level atom with resonant atomic frequency ω_o being illuminated by a laser of frequency ω_l. The laser is detuned with its frequency ω_l below the resonant frequency ω_o with $\Delta E < 0$.

I noted in Section 2.1 that an atom receives a momentum kick in the direction of the inbound photon (laser) when it absorbs a photon and gets promoted to an excited state. This kick is very small for the atoms (of order $10^{-}28$ kg·m/s from a photon compared to the experiment's atomic momentum at thermal velocity of order $10^{-}23$kg·m/s) [16]. However, the atoms recoil due to collisions with millions of photons which has the cumulative effect of pushing the atom away from the laser that is illuminating it. The atoms also receive a momentum kick from photons released during spontaneous emission, but as they are released in random directions, the cumulative effects from spontaneous emission average to zero and result in no net change in momentum. Due to the Doppler shift, momentum exerted from the photons is proportional to the atom's velocity, and opposes the motion of the atom when the laser is tuned below atomic resonance as shown in Figure 2.2 [16].

The preceding discussion is based on the momentum transfer between photons and atom resulting in forces on atoms. Here, I discuss the cooling process. The cooling process relies on conservation of energy. With the detuning set below resonance, the absorbed photons have a smaller energy than the emitted ones ($E = \hbar\omega_l$ vs $E = \hbar\omega_o$). However, energy must be conserved and so the difference in energy is made up from the kinetic energy (motional energy) of the atom. The result of this energy difference is that the atoms lose energy during this process and over time the atom slows down considerably in the direction of the lasers. The effect works for many different velocity groups and eventually "piles" up the atoms into one group. Since the spread of this final group is small, this is known as "cooling". Although "slowing" is a statement about velocity and "cooling" is a statement about "velocity spread", in this case I refer to both the cooling and slowing process as cooling because the loss of energy affects both metrics. This phenomenon is also called an optical molasses as the atoms act like they are moving through a viscous, molasses-like fluid.

The final aspect of the MOT involves a discussion of how the atoms are localized. The localization is caused by the "magnetic" part of the MOT. I accomplished this by placing four permanent magnets in a quasi anti-Helmholtz configuration around the rubidium chamber that now consists of an optical molasses. The force of these magnets on the atoms relies on the position of the atoms and increases linearly the farther from the center of the MOT the atoms are in the direction transverse to the desired direction of the atomic beam. The combination of this magnetic field with the proper circular polarization of light from the cooling laser causes a force that is spatially dependent. When an atom in such a magnetic field is subjected to two counter-propagating laser fields, the Zeeman shift causes the atom to "see" the laser opposing its motion to be closer to resonance and the laser propagating with the atomic velocity to be shifted away from resonance. The next imbalance pushes the atom back to the center. In my system, the resulting atomic beam is aligned with a small pinhole leading to the main vacuum chamber. Figure 2.3 shows an infrared image of my MOT.

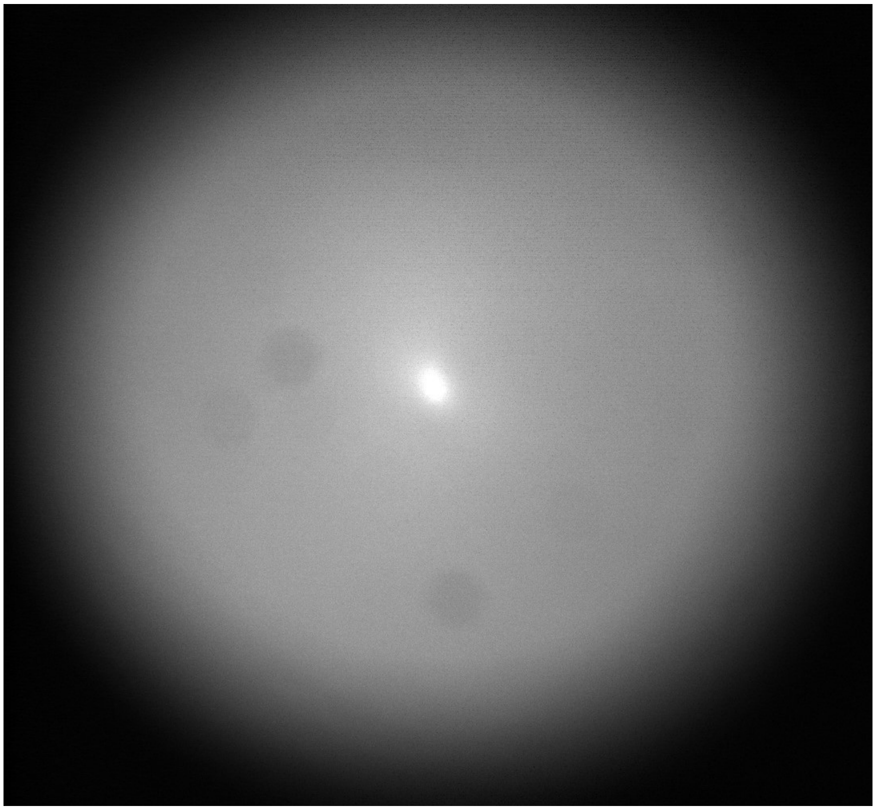

Figure 2.3. Infrared photograph where the bright white florescence in the center is the 2D MOT. The photograph is angled along the x-axis where the atoms are free to traverse along into the main vacuum chamber.

2.6 Repumping

So far I have considered phenomena that can be mapped onto a simplified two level atom. However, the ^{85}Rb atoms I use are broken into many different fine (granularity not quality) and hyperfine energy levels, with the relevant energy levels for the experiment being the ground ($5^2S_{1/2}$) and excited ($5^2P_{3/2}$) states, with the latter's hyperfine levels denoted by F'. This transition is known as the D_2 transition for ^{85}Rb and is shown in Figure 2.4. The difference between the fine and hyperfine structure is that hyperfine includes total nuclear angular momentum **I** along with total electronic angular momentum **J**, which in turn is composed of orbital angular momentum **L** and spin angular momentum **S**. The previously described cooling process is normally done on the $F = 3$ to $F' = 4$ transition, although others can be used. Due to this added complexity, I can no longer use the two-level analogy. While this this more complete picture is more accurate, it also highlights a problem. When a laser is tuned close to this cooling transition, there is a nonzero probability of exciting atoms to the $F' = 3$ state instead of the $F' = 4$ state. This probability is around $\frac{1}{1600}$, and the $F' = 3$ state has has a branching ratio of about 50% [16]. Thus, after on average 1600 cycles, the atom accidentally gets excited to the $F' = 3$ level, where there is an equal probability of decaying to the $F = 3$ state or the $F = 2$ state. If it decays into the $F = 3$ state, the cooling continues uninterrupted. However, if the atom decays into the $F = 2$ state, the cooling process stops. In order to circumvent this problem, I relied on a process called repumping that promotes the atoms back into the $F = 3$ state. As previously discussed the $F = 2$ to $F = 3$ direct transition is dipole forbidden and cannot be directly driven. Furthermore, selection rules prohibit the $F = 2$ to $F' = 4$ transition ($\Delta F = \pm 1$ or 0). What I dis instead is tune a second laser to the $F = 2$ to $F' = 3$ transition which serves to give the atoms another 50% chance to decay in the $F = 3$ state allowing the cooling process to continue.

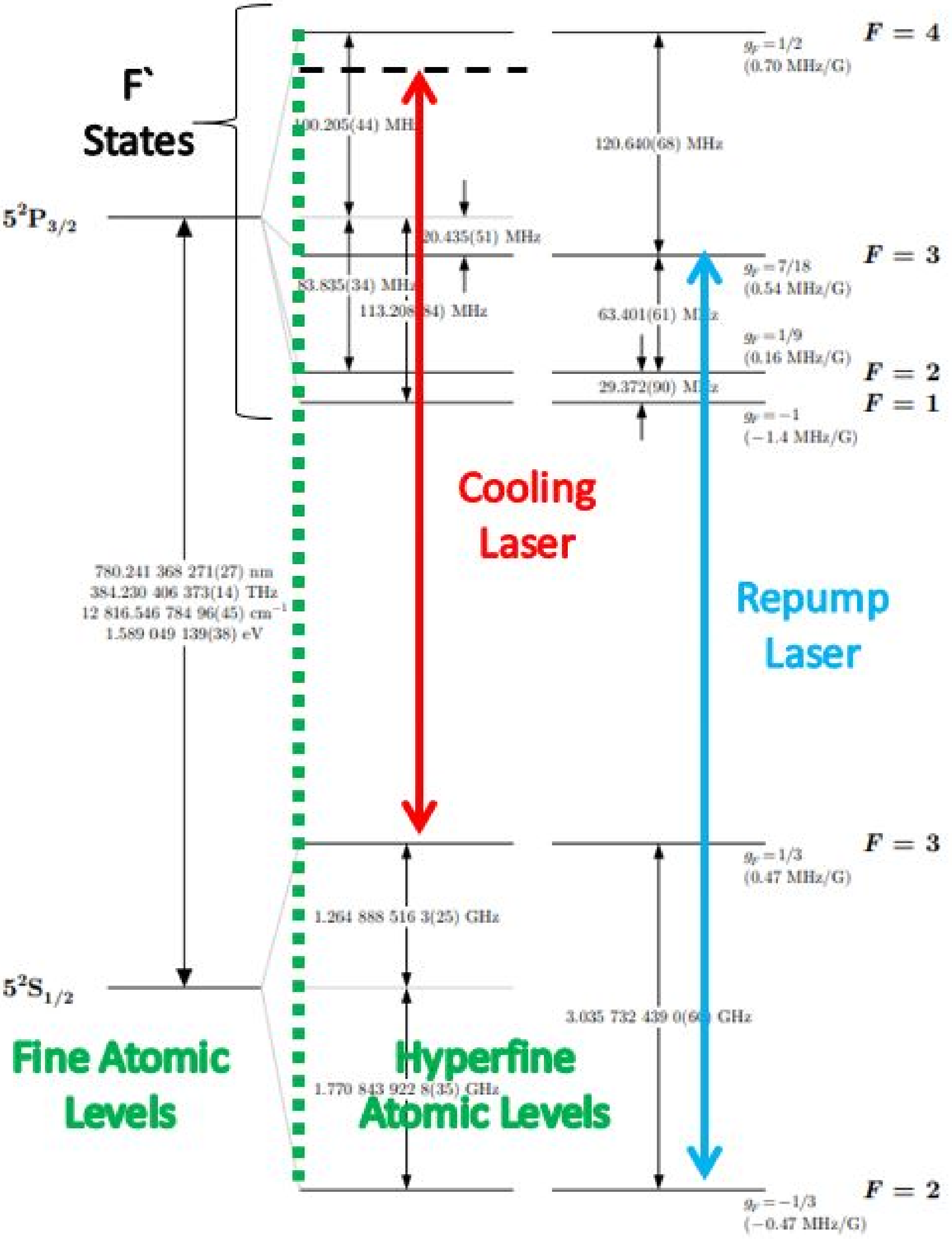

Figure 2.4. $^{85}Rb\ D_2$ transition hyperfine energy level structure, with frequency splittings between the levels. Highlighted are the cooling and repump transitions discussed in this chapter. Also of note is the roughly 780nm separation between these two fine energy levels. Source: [35]

2.7 Detection

The key aspect of this experiment is measuring the specific quantum states of the rubidium atoms. This process involves illuminating the atom beam with light from a third laser that I refer to as the detection laser, and collecting spontaneously emitted photons with a photomultiplier tube (PMT). As noted in Section 2.6, the atom beam contains atoms in an incoherent mixture of atoms in the two different hyperfine ground states, $F = 3$ and $F = 2$. Due to poor atomic properties the $F = 2$ state is hard to measure. Because the population must be conserved and therefore must be in either the $F = 2$ or $F = 3$ state, it is sufficient to measure the $F = 3$ state and infer the population in the $F = 2$ state. This was done by tuning the detection laser to a frequency equal to the $F = 3$ to $F' = 4$ transition. When atoms in the $F = 3$ state were illuminated by the detection laser they were excited to the $F' = 4$ and, after a brief amount of time, decayed back to the $F = 3$ state and released a photon through spontaneous emission. A negligibly small fraction of atoms were excited into the $F' = 3$ state and decayed into the $F = 2$ ground state without any emission. Also, any atom that passed through the laser not in the $F = 3$ ground state was not promoted to the excited state and therefore not measured. This process measures the number of atoms in the $F = 3$ state by having the PMT detect a portion of the spontaneously emitted photons from the atoms decaying from the $F' = 4$ to the $F = 3$ state.

2.8 Optical Pumping

After the cooling and repumping processes, atoms exiting the MOT are in an incoherent and uncontrolled mixture of the two ground states. However, I need the atoms leaving the MOT to be in the $F = 2$ ground state to unambiguously perform measurements during the experiment. Previous research modeling showed that only a small, but not negligible, fraction of atoms are in the $F = 2$ state after they pass through the MOT lasers and decay [36]. I "initialized" the system and put all the atoms into the $F = 2$ state through a process called optical pumping. This involves passing the atoms through a specifically tuned laser before they enter the main vacuum chamber that places them in the $F = 2$ state. Unfortunately, the necessary frequency for the transition from the $F = 3$ to the $F = 2$ state is in the microwave range, and I do not have the needed equipment. Instead, I relied on pumping the atoms to an excited state and had them decay to the state I want. Previous research again lights the way by showing that driving the $F = 3$ to $F' = 2$ transition will provide the most efficient way to *optically pump* the atoms into the $F = 2$ ground state [16].

2.9 Simulations

Many effects can weaken or destroy the results I am hoping to observe, and to that end, I used a MATLAB code that I modified to take many of my experimental variables into account including the spread in velocity of the atoms, divergence of the atomic beam, and the intensity profile of the laser to provide qualitatively and quantitatively accurate representations. These provided helpful guides for improving and characterizing my results and understanding the effects individual variables had on the experiments.

2.9.1 Rabi

I first ran simulations of the Rabi oscillations that I measured by varying the Raman field's power. Rabi plots show the oscillations in probability of atoms being in the excited state ($F = 3$). These oscillations are strongest when the laser is tuned to atomic resonance. I wanted to understand how two variables affected the oscillations. The first variable was the velocity spread of the atoms, or velocity averaging, and the second was the angular divergence of the atom beam. The results are displayed in Figure 2.5 using values for the parameters of the simulations that I had previously measured as inputs. Specifically, I considered an angular atomic divergence of 128mrad, a most probably velocity (V_{mp}) of 20m/s, and location of the Raman fields from the MOT of 14mm. The simulations were normalized to the $\pi-$ pulse condition for a laser beam of finite width assuming $V_{atoms} = V_{mp}$. When I did not include velocity averaging or angular divergence I found a simple cosine curve (Figure 2.5(a)) that reflects the atoms moving in between the ground and excited states. When I included velocity averaging the oscillations dampen out (Figure 2.5(b)) and shift the first peak to a slightly higher $\pi-$ pulse factor. When just angular divergence was added there was barely any discernible change (Figure 2.5(c)) although from closer inspection, there is a slight compression of the oscillations. When both variables were included (Figure 2.5(d)) a near mirror image of the velocity averaging only curve is predictably produced. These results show that the dominant effect on the Rabi cycling is the velocity averaging, while accounting for the atomic beam divergence has a negligible effect. Despite the washing out of the Rabi oscillations, enough of the oscillations remain to determine the π condition.

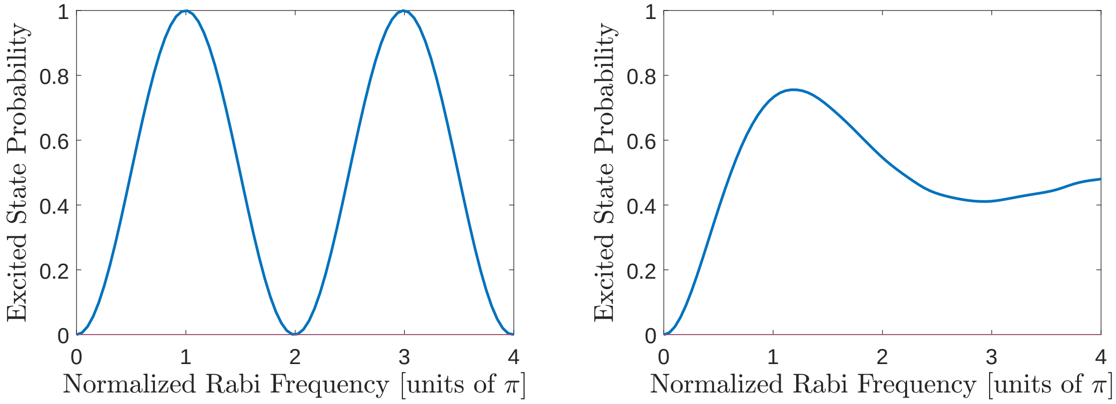

(a) Rabi

(b) Rabi with velocity averaging

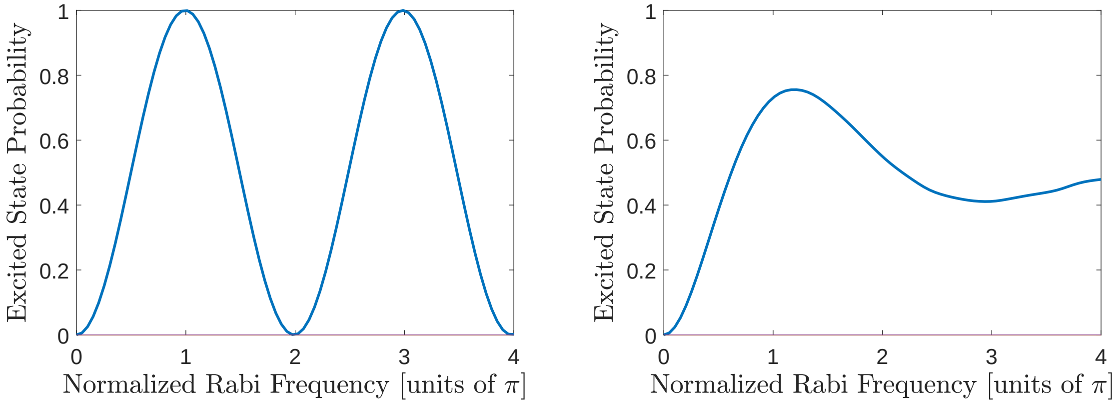

(c) Rabi with angular divergence

(d) Rabi with both variables

Figure 2.5. Figure (a) displays ideal Rabi oscillations where the atoms oscillate in between the ground (0) and exited state (1), figure (b) shows the oscillations with velocity averaging added, figure (c) depicts the oscillations with angular divergence added, and figure (d) provides the oscillations with both velocity averaging and angular divergence added.

2.9.2 Ramsey Interference

I next ran several simulations to characterize what interference patterns I could expect from a Ramsey configuration of two $\pi/2$- pulses. I was interested in how velocity averaging and the divergence of the atom beam also affected the interference. Figure 2.6 contains simulation results from the co-propagating configuration without and with velocity averaging (Figure

2.6(a) and (b) respectively). I did not include angular averaging due to the fact that the Rabi simulations showed it had little affect.

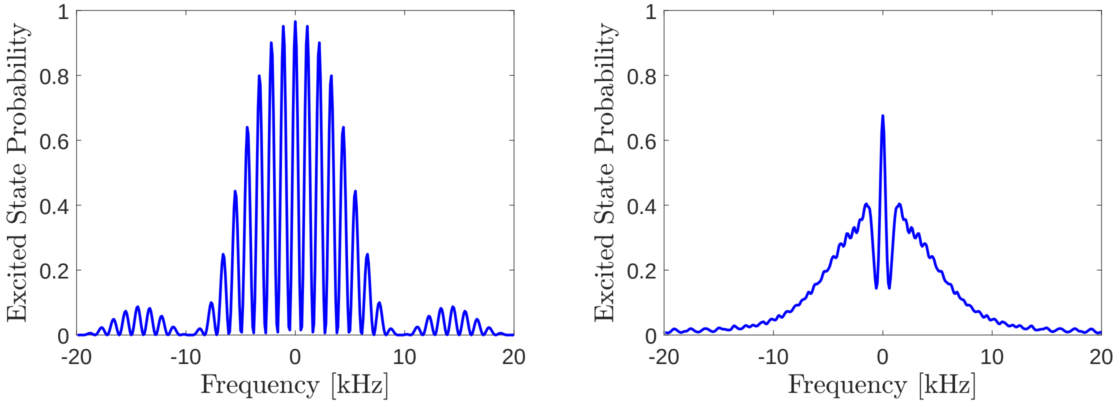

(a) Ramsey without averaging

(b) Ramsey with velocity averaging

Figure 2.6. Figure (a) is the co-propagating Ramsey spectrum without velocity averaging and Figure (b) is the Ramsey spectrum with velocity averaging. A simulated slit spacing of 20mm was used.

A useful measure of the quality of an interference spectrum is known as the contrast, defined by

$$Contrast = \frac{Amplitude_{peak} - Amplitude_{trough}}{Amplitude_{peak}}, \tag{2.11}$$

where the peak can be either the center peak or one of the secondary peaks. The Ramsey simulations were then repeated for the counter-propagating configuration. These results are shown in Figure 2.7, in the same layout as Figure 2.6. Here I found that the velocity averaging had a similar effect as in the co-propagating case. In contrast to the co-propagating case, the atomic divergence had a significant effect on the interference. The divergence impacting the interference is a result of the fact that the counter-propagating situation is very sensitive to the transverse velocity components.

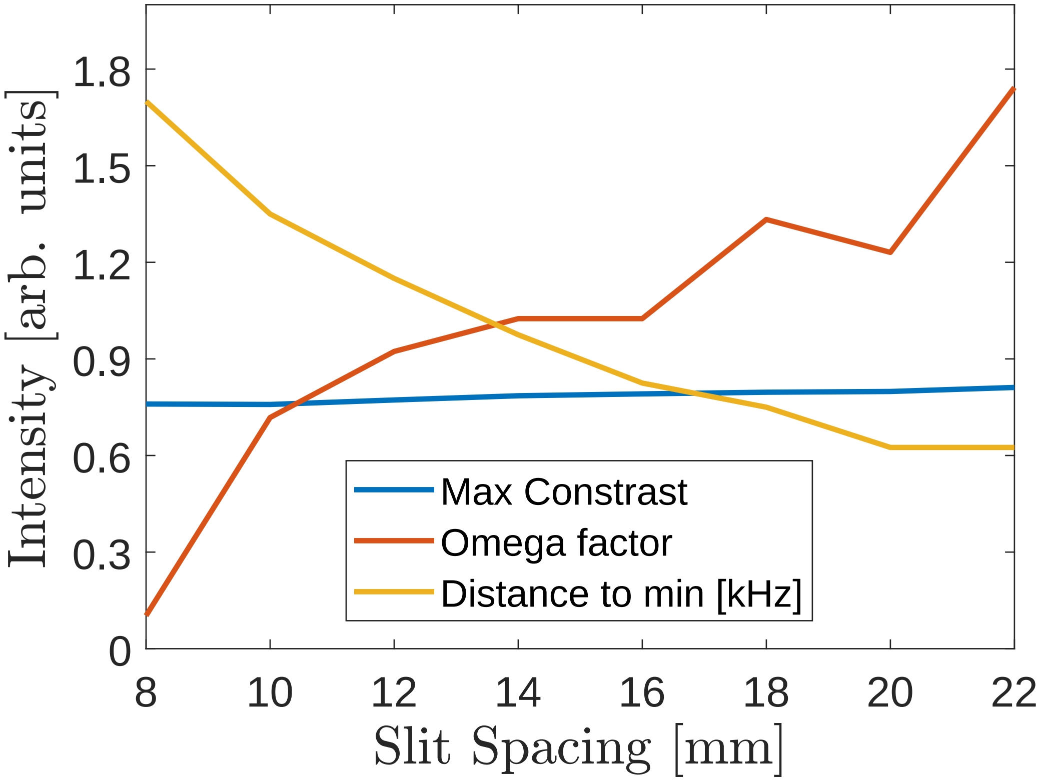

Figure 2.7. The Figure shows how the max contrast of the peaks (blue) increases marginally as slit spacing increases. It is also shown that the scaled intensity of the laser (Omega Factor-red) where the best contrast occurs increases with slit spacing. Meaning that the wider the slits, the greater laser power needed for best contrast. The third curve (yellow) shows how the distance from peak to trough decreases with larger slit spacing which matches what the theory.

Figure 2.8 shows how in a counter-propagating configuration, angular divergence of the atom beam has a significant effect.

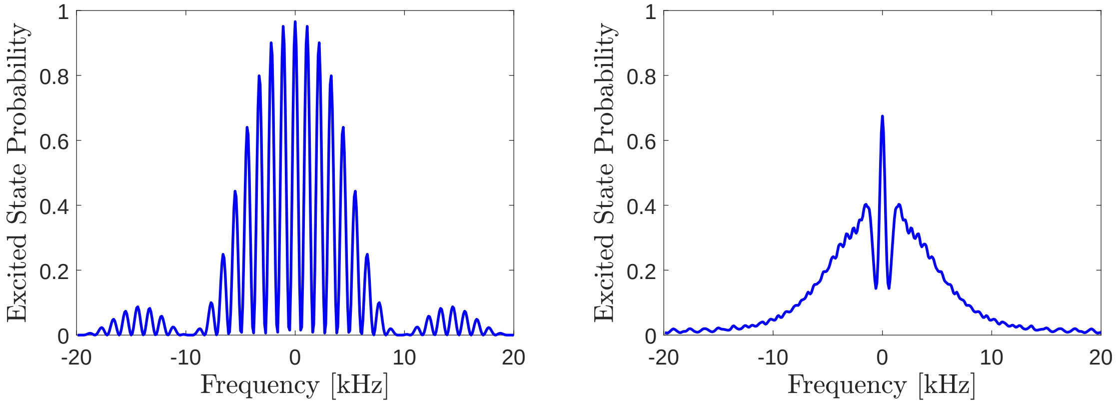

(a) Ramsey

(b) Ramsey with velocity averaging

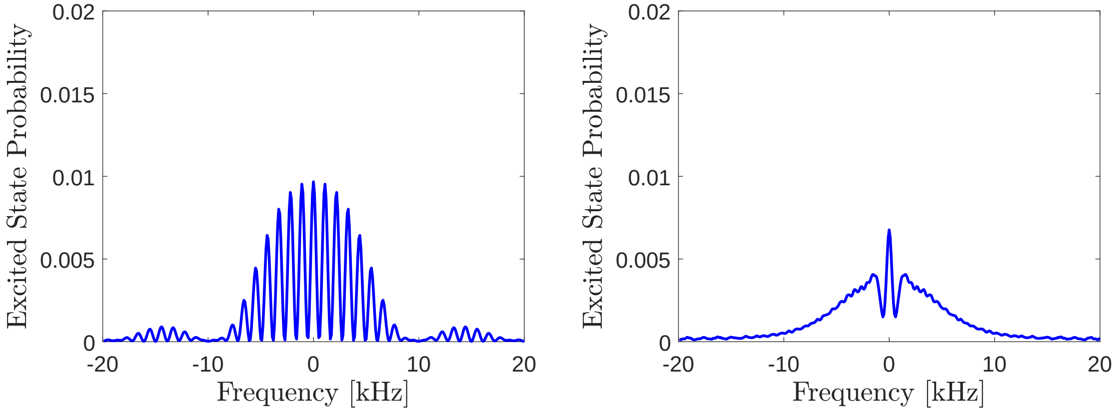

(c) Ramsey with angular divergence

(d) Ramsey with both variables

Figure 2.8. Figure (a) displays ideal counter-propagating Ramsey interference, figure (b) shows counter-propagating Ramsey with velocity averaging added, figure (c) depicts counter-propagating Ramsey with angular divergence added, and figure (d) provides counter-propagating Ramsey with both velocity averaging and angular divergence added. I change scales for figures (c) and (d) due to the strong effect of the angular divergence.

2.9.3 Spin Echo Slit Spacing

The full interferometer is composed of two $\pi/2-$ pulses with a $\pi-$ pulse in between separated by free evolution time. I call this interference set up "spin echo." In order to produce this, I needed a mask with three slits instead of the two I used for Ramsey interference. I created a

MATLAB program that would calculate the location of a slit 2 mm wide within a Gaussian laser field of a given $1/e$ width (which I measured) when a 2 mm slit in the center has sufficient power to produce a π- pulse. From the code, I found that the slits need to be separated by approximately 9.2 mm. The full variation of the ratio of power in the side slits with respect to the center slit is shown in Figure 2.9.

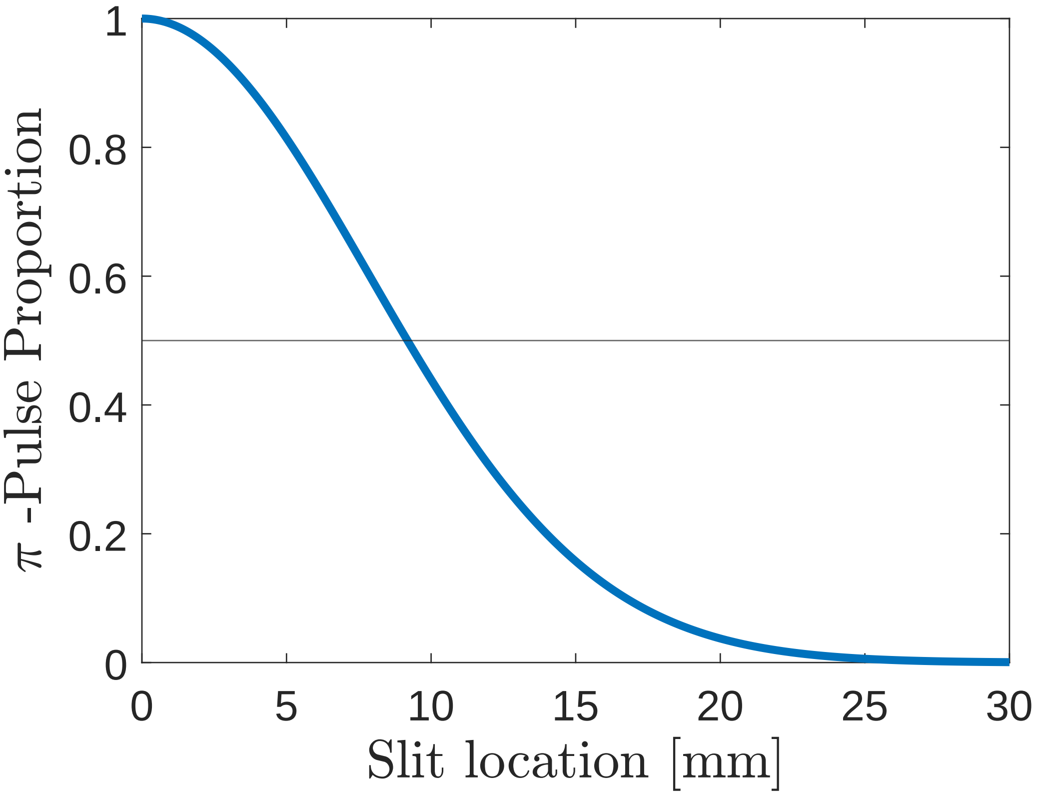

Figure 2.9. Curve resulting from calculation of slit spacing for Gaussian bean in terms of proportion of a $\pi-$ pulse. Intersection of two curves occurs at $\approx$ 9.2mm for $\pi/2-$ pulse.

THIS PAGE INTENTIONALLY LEFT BLANK

CHAPTER 3:
Experimental Setup

In this chapter, I discuss the experimental apparatus that I used to perform the experiments that I cover in Chapter 4. In the following sections I focus on the setup of the lasers and the interferometer, highlighting the MOT, saturated absorption setups, and the detection of the atomic states of the atoms.

3.1 Apparatus Design

The previous chapter described how I cooled and trapped atoms to create a 2D MOT. This effect was produced using a part of the apparatus I termed the "cooling arm." As shown in Figure 3.1, this complex arrangement of optics polarizes and directs light into a chamber containing gaseous rubidium. The light, which is a mixture of cooling and repump light (see Chapter 2) passes through several optics before illuminating the rubidium atoms from four directions with the help of beam splitters and retro-reflecting mirrors in the arrangement shown in Figure 3.1. There are also four permanent magnets around the MOT chamber that produces a magnetic field gradient along the direction of propagation of the lasers, but none in the direction with no laser beam. This geometry results in a sample of atoms that are cooled in the direction along the laser beams by laser cooling but not along the direction longitudinal to the atom beam.

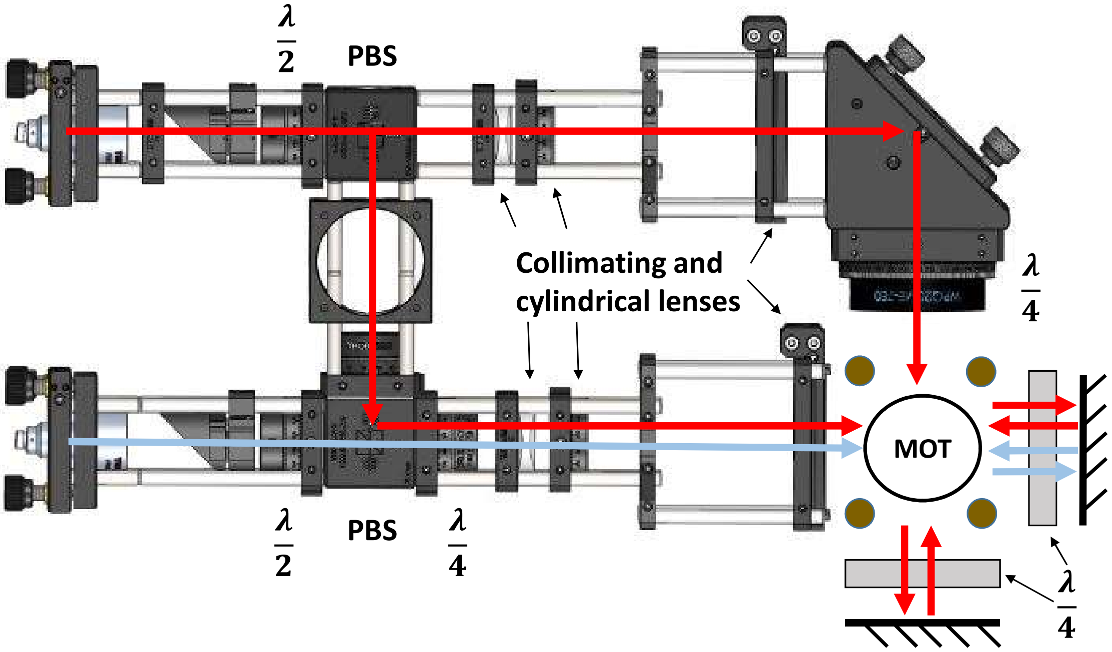

Figure 3.1. Schematic of the cooling arm and MOT including optical paths of the two lasers (red is cooling and blue is repump) including waveplates, shaping optics and mirrors.The four brown circles represent the 4 permanent magnet bars viewed from the back side (i.e., the atoms are propagating into the page).

The MOT chamber is connected to the main vacuum chamber via a small hole. This allows atoms to leave the MOT creating an atom beam that propagates through the main vacuum chamber. As seen in Figure 3.2, the vacuum chamber consists of three symmetric sets of three windows that are used for lasers or sensors or are blacked out as needed. In Figure 3.2, the atoms travel leftwards from the MOT chamber. I performed the interferometry in the center (2nd) window and my detection in the window farthest from the MOT (3rd window).

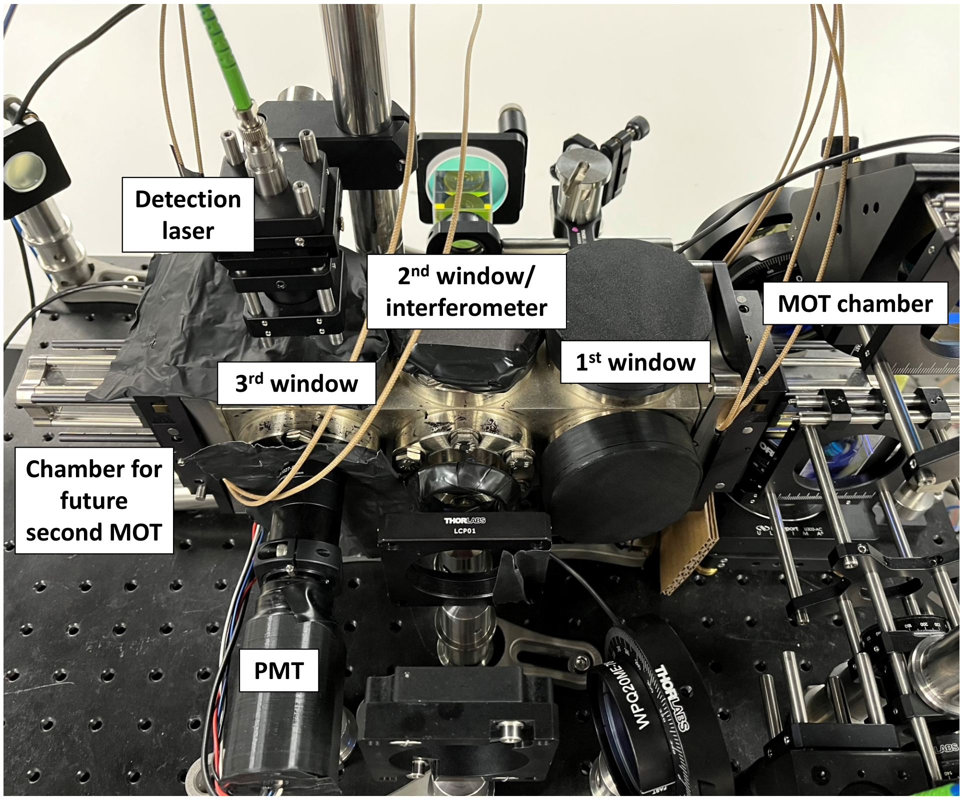

Figure 3.2. Image of main vacuum chamber with tower and MOT on the right. The center window is covered up with my interferometer setup, and the left section has the detection laser in the vertical window and the PMT in the horizontal window. A gas chamber for a potential second MOT is on the far left.

3.2 Saturated Absorption

The light that is used in this experiment comes from semiconductor diode lasers that produce light at 780nm which is the resonant frequency for rubidium atoms. Specifically, it is the frequency difference between the two fine states of the D_2 transition. However, the frequency of the light from these diodes needs to be tuned properly, stabilized, and monitored during the experiment.

The primary method of determining the frequency of the light is through Doppler free saturated absorption spectroscopy. The optical setup is shown in Figure 3.3. I need to lock the lasers at certain frequencies and spectra produced by Doppler free spectroscopy are used to visually determine the frequency of the lasers as a function of the control parameters. These spectra are generated by passing two parallel beams through a rubidium gas cell onto a two-sided detector. One beam is a single probe beam that passes straight through the rubidium to the detector, which measures the Doppler broadened transitions. The second beam is composed of a forward propagating probe and a backward propagating pump beam, which is incident on the other side of the two-sided detector. It registers the same Doppler profile but with spectral holes "burned" into the profile at the frequency of the naturally occurring resonances. The signal from the single probe is subtracted electronically from the signal from the pump/probe combination to remove the Doppler curve, leaving just the transition peaks. This method allowed me to see the saturated absorption spectrum of four rubidium energy levels: the $5^2S_{1/2}$ (cooling) and $5^2P_{3/2}$ (repump) transitions for the ^{85}Rb and ^{87}Rb isotopes (I do not use the ^{87}Rb isotopes in my experiments). The eponymous cooling and repump lasers are tuned to their respective transitions of the ^{85}Rb isotope, as they are the relevant ones for my research. The detection laser is also tuned to the cooling transition so it can measure the atoms in the $F = 3$ state after they pass through the Raman fields serving to make the atom optic beams, which will be explained shortly. Figure 3.4 displays the cooling transition saturated absorption spectrum.

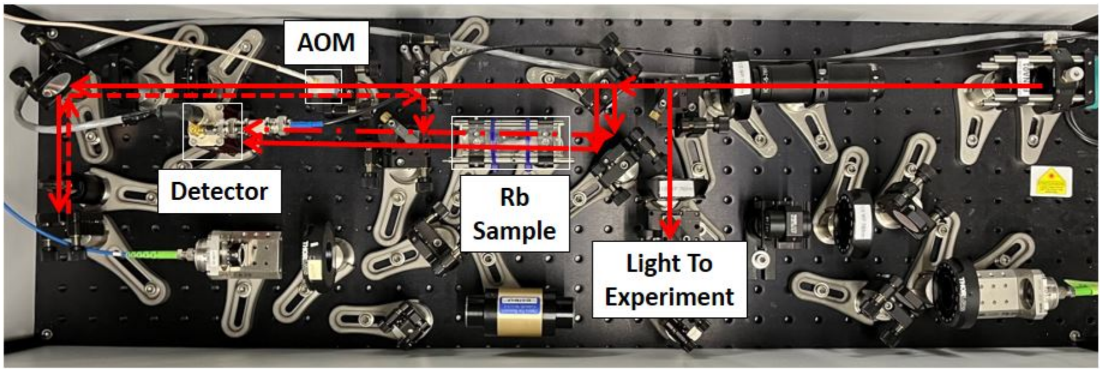

Figure 3.3. Overhead photograph of a saturated absorption setup with optical paths for the probe and pump beams. The uniform dashed line is the retro-reflected AOM beam, and the nonuniform dashed line is the pump and probe beam.

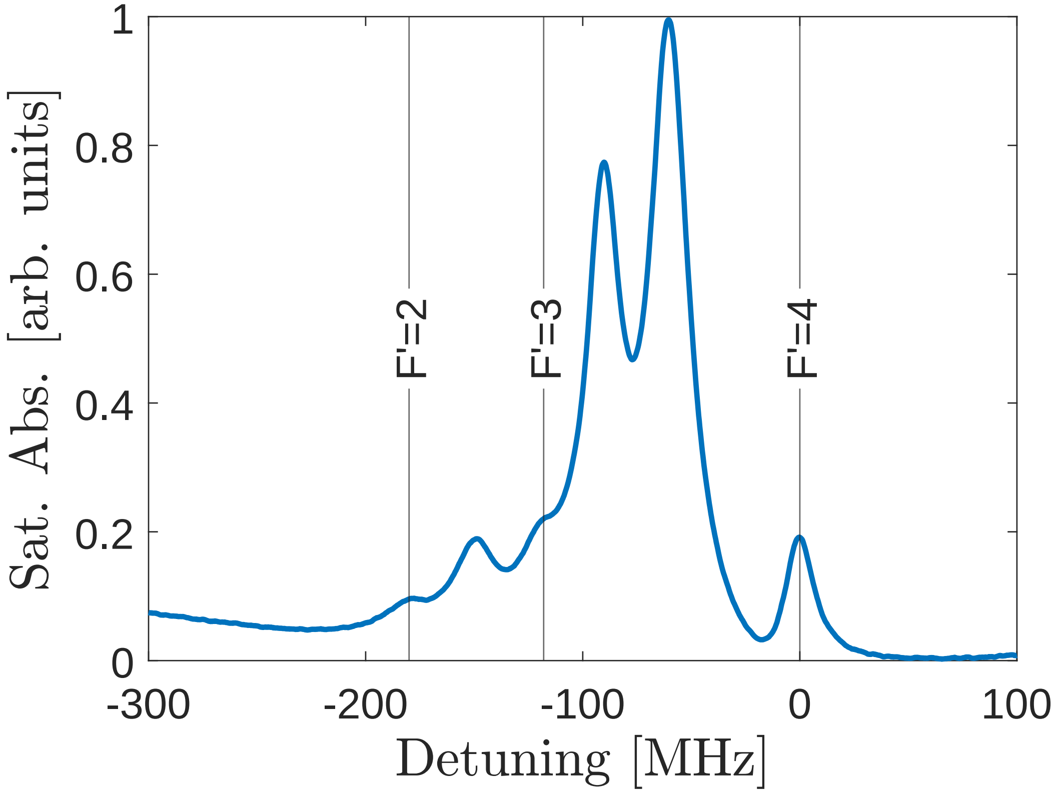

Figure 3.4. Scan of the saturated absorption spectrum for the cooling transition with zero being defined at the $F = 3$ to $F' = 4$ transition. The non-labeled peaks are the result of crossover resonances which are not covered in this paper. See reference [37].

3.3 Experimental Parameters

In order to produce the best possible results, I needed to properly characterize the atomic beam profile, specifically the angular divergence and the velocity of the atoms. Previous work had performed these characterizations, but due to changes in the apparatus and desire for replicability I needed to perform the characterization again.

3.3.1 Signal Optimization

My metric for optimizing the system was the signal from the detection laser. The detection process is described in detail in Chapter 2. The detection laser is located in the furthest window from the MOT in the vacuum chamber and propagates vertically down (with a slight angular offset to avoid scattering from the windows and to spectrally separate the signal from the laser cooled atoms from the small residual signal from hot atoms leaking out of the pinhole). The photon emissions stimulated by this laser are captured by a sensor positioned horizontally in the far windows. This sensor is a PMT that receives input in the form of photons which create a tiny current that is then multiplied thousands of times to provide a macroscopically large signal. The PMT output is displayed on an oscilloscope as a voltage after going through a transimpendance amplifier and appears as a peak when the laser is scanned through resonance. Figure 3.5 shows a plot of the detection peak overlaid on the saturated absorption scan. Notice the detection peak does not align with the cooling transition peak in the saturated absorption. This shift is due to a frequency shifter in the detection laser setup. This signal is then optimized by improving the signal to noise ratio (SNR), which is calculated by the height of the Lorentzian peak above the background value of the signal divided by the background.

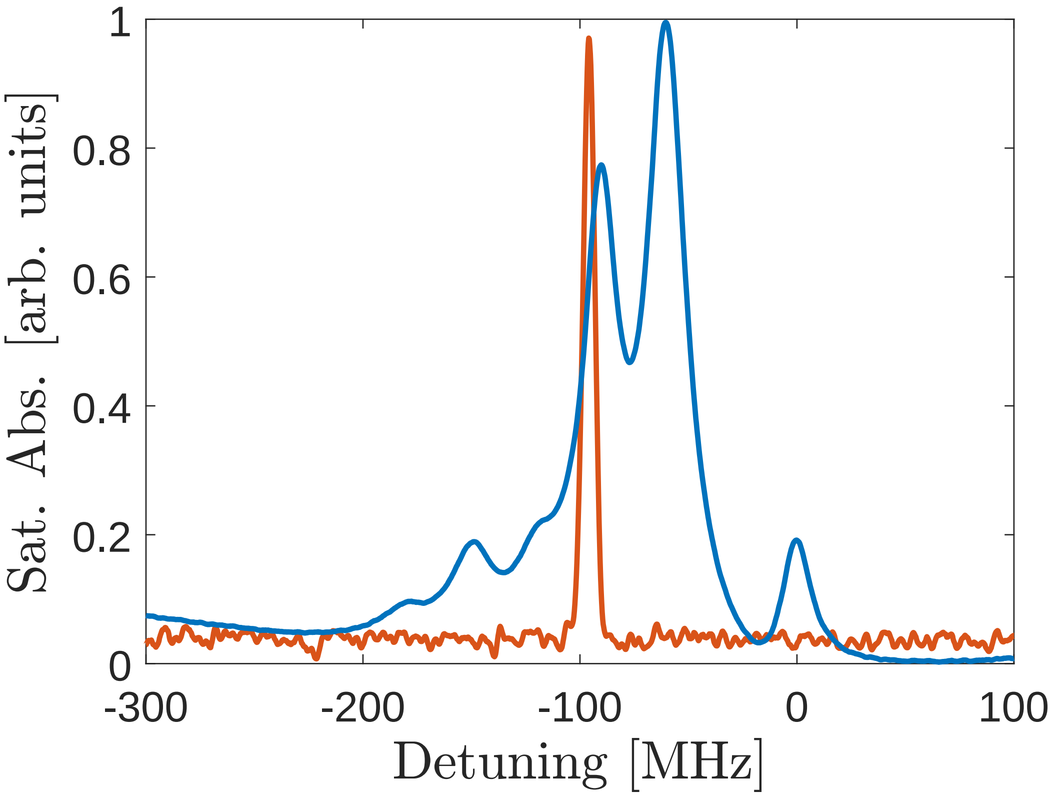

Figure 3.5. Scan of the PMT signal (red) and cooling transition (blue) overlapped at the new lock-point that had been shifted ≈ -90 MHz by the AOM.

There are several techniques to improve the SNR and optimize the signal. First, background light can be reduced by covering the unused vacuum chamber windows and blocking beams in order to reduce unwanted scattering. Manual adjustment to the atomic beam trajectory can be made. The location of the MOT can be adjusted to better align with the hole connecting to the main vacuum chambers by translating the pinhole. The efficiency of the laser cooling can also be optimized by moving directional knobs on the fiber optic couplers in the tower as well as on the different mirrors. Ensuring the detection laser is centered on the atom beam will also improve the signal. Increasing the cooling laser power is another way to improve the signal, which can be done via a tapered amplifier that amplifies the cooling light. These adjustments were all made while monitoring the signal above background on the oscilloscope to optimize the signal in real time.

Another method to improve the SNR is to manually change the laser detuning by adjusting the lock point on the saturated absorption spectrum to find the best SNR. However, for my experiments I lock to the $F = 3$ to $F' = 4$ transition within the saturated absorption spectrum. As seen in figure 3.2 and 3.5, this transition produces a small peak in the saturated absorption spectrum, and any instability can cause the laser to break lock. I overcame this by adding AOMs to my detection and cooling laser sets ups. These modulators work by shifting the frequency of light that passes through it. I configured the path of the laser to pass through twice thus doubling the amount I can shift the lock point. For my experiment, I was able to shift the laser frequency in such a way that the proper locking point is on the larger peaks, allowing for minor instabilities without breaking lock.

3.3.2 Atom Beam Characterization

The first step of characterizing the atom beam is to optimize the getter current (the source of rubidium). I established that the optimal current on the getters is 2.4 Amps. This optimization was determined determined by measuring the SNR as described before for varying values of the getter current. These results are found in Table 3.1.

Table 3.1. Getter Current settings and corresponding signal to noise ratios showing 2.4 Amps to be the optimal current setting.

Current [A]	SNR
2.1	2.76
2.2	3.81
2.3	5.10
2.4	6.01
2.5	4.63

The width or divergence of the atom beam as it propagates through the vacuum chamber is the second phase of characterization. I measured this by first illuminating the atom beam with repump light (only) in the first window after the MOT which optically pumps all of the atoms into the $F = 3$ state. I then placed an infrared camera in the third window perpendicular to the detection beam to capture the spontaneous emissions from the atoms that passed through the detection beam. I calculated the angular divergence from

$$\phi = \arctan(\frac{W_{fl} - W_p}{l}) = 0.1281 rad, \tag{3.1}$$

where ϕ is the angular divergence, W_{fl} is the width of the florescence in the detection laser (31mm), W_p is diameter of the pinhole (1mm), and l is the distance from the pinhole to the detection laser (233mm). However, as Section 2.2.1 notes, the angular divergence does not have much effect on the co-propagating experiments I conducted, but proves to be a critical parameter in the counter-propagating experiments.

The last aspect of the atom beam I characterized was the velocity of the atoms. The atoms velocity profile is described by the usual Maxwell-Boltzmann distribution, which is characterized by a single parameter—the most probably velocity, V_{mp}. One method to measure this is to direct a scanning near-resonance laser backwards along the atomic beam trajectory and measure the Doppler shift with respect to the Doppler-free saturated absorption line. However, previous work [16], [25], [36] found that the Doppler shift was too small to provide a reliable measure of V_{mp}. Instead, I accomplished this by pulsing the optical pump beam off for a range of times (2ms to 20ms) which would allow a small segment of atoms in the $F = 3$ state through before resuming moving atoms to the $F = 2$ state again. A measurement of the fluorescence from the locked detection laser is a curve depicting atoms passing through the detection laser as a function of time. Figure 3.6 shows a representative curve for a 5ms long optical pump "off" time. I fit each curve to a modified Gaussian function where V_{mp} is one of the fitting parameters. I plotted the resulting V_{mp} for each pulse width I tested in Figure 3.7 and fit the data to the best fit line showing that for an ideal pulse (which occurs for an infinitely short pulse) $V_{mp} \approx$ 20m/s. Given knowledge of the Maxwell speed distribution equation and noting that the *effective* temperature of the 2D MOT cell is approximately 1000 K, intuition may lead us to think the V_{mp} should be much higher, but this relatively low velocity could be a result of the cooling of the atoms in the MOT which only allows for slower atoms to propagate through.

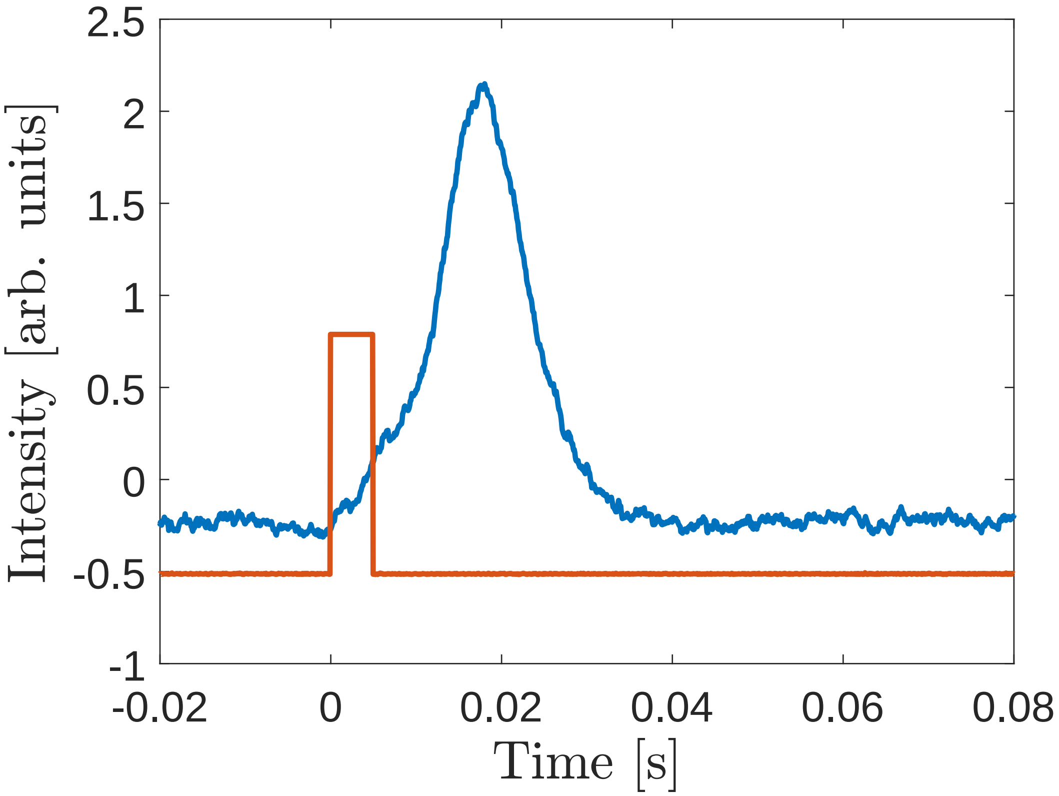

Figure 3.6. Florescence from the detection laser over the optical pump pulse which produces a spread of atoms over time. This combined with the distance traveled by the atoms allowed me to calculate the velocity profile. The top of the peak is produced from the largest grouping of atoms and serves as a rough measure of the most probably velocity, which was more precisely extracted by the fitting routines.

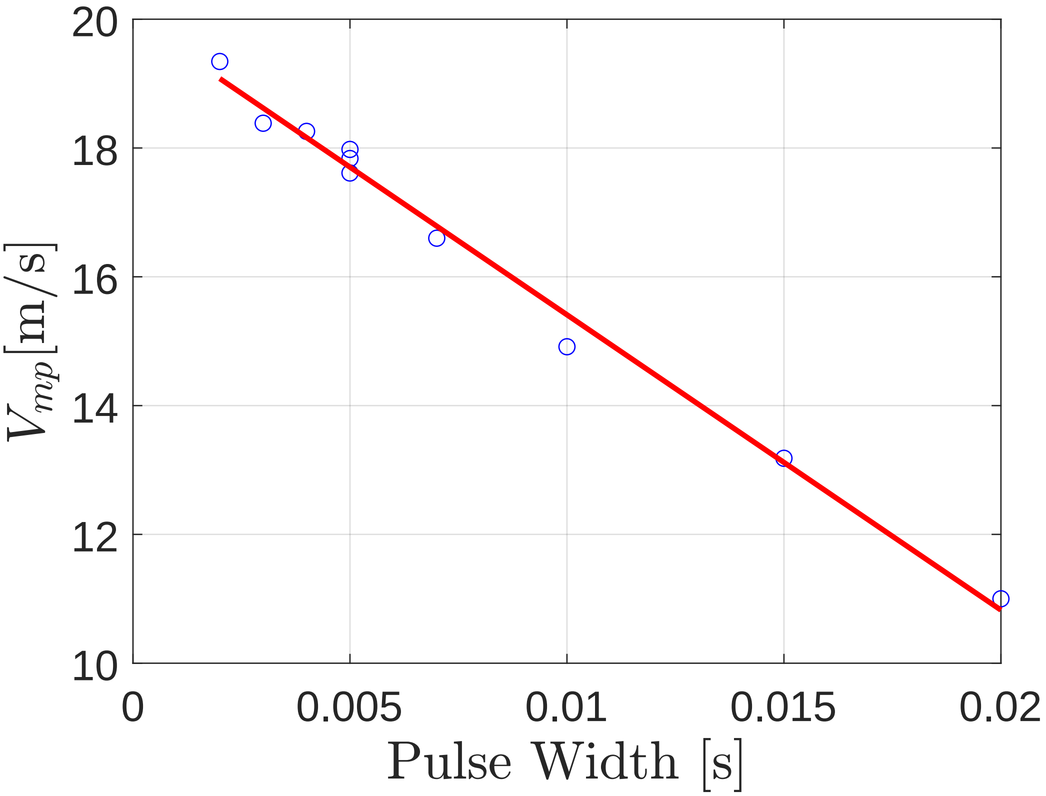

Figure 3.7. Plot of V_{mp} versus pulse width with a linear fit. Plot shows that as we move to an ideal pulse (instantaneous) V_{mp} approaches ≈ 20m/s.

Figures 3.8 and 3.9 show two of the Gaussian fits, corresponding to pulse widths of 20ms and 2ms respectively. We can see that the 2ms fit is much better—a trend that holds for all the short pulses. The change in scale between the two graphs is due to the smaller number of atoms that are able to move through the gate during the shorter pulse. I hypothesize that the shoulder on the front end of the signal peak in Figure 3.7 is the result of fast atoms not trapped in the MOT.

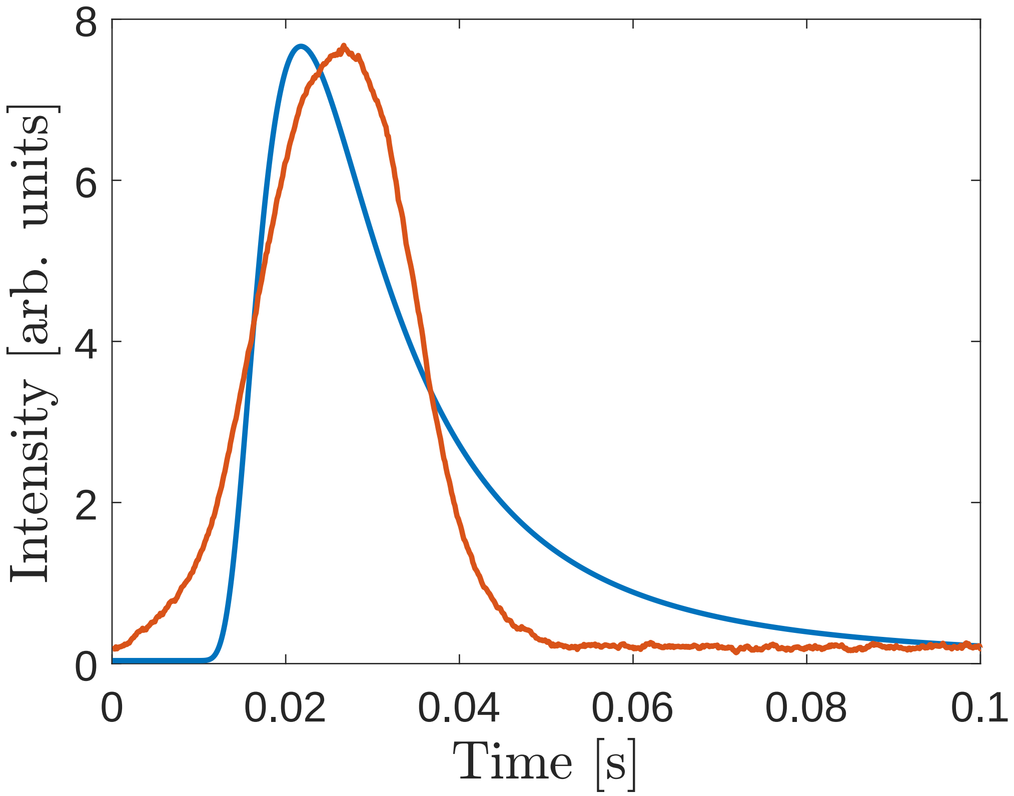

Figure 3.8. Less than optimal Gaussian fit (blue) to the velocity profile of the atoms (red) taken for a pulse of 20ms.

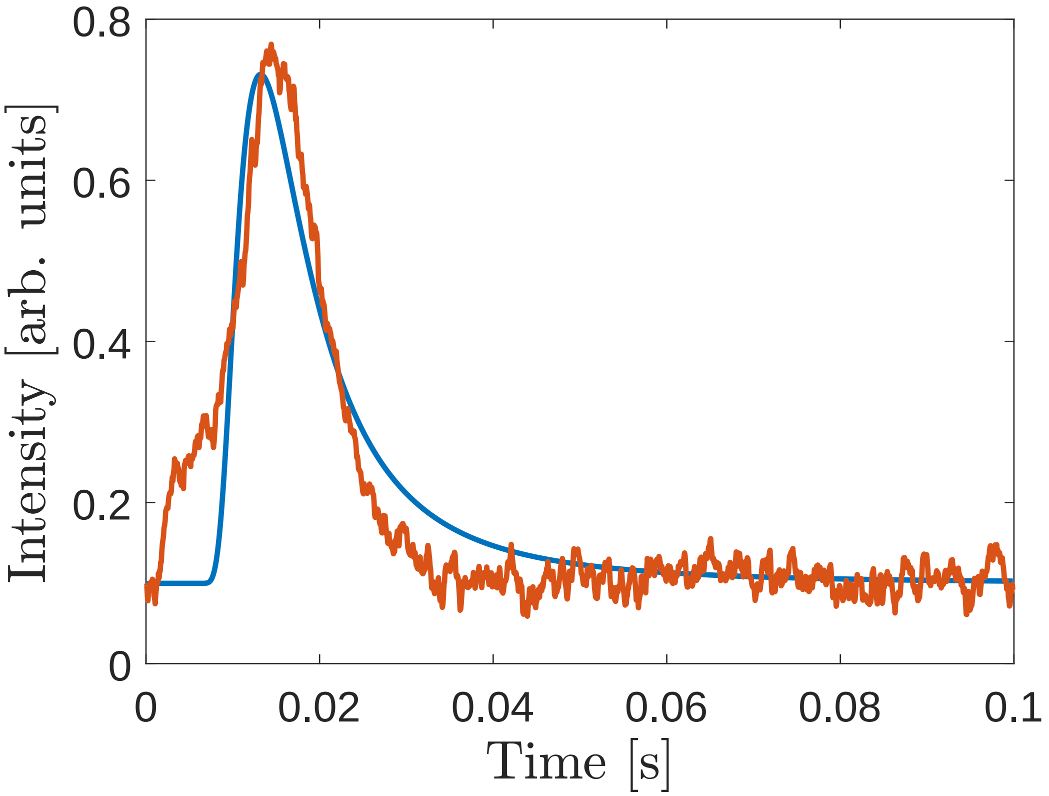

Figure 3.9. Moderately improved Gaussian fit (blue) to the velocity profile of the atoms (red) for a gate 2ms vs the previous 20ms fit.

3.4 Lock-in Detection

When detecting fluorescence from a Raman process, the maximum signal achievable is 20% of the total fluorescence (due to the fact that the $F = 2$ ground state has $2F + 1 = 5$ magnetic states and a Raman process only utilizes one state) [36]. This creates a small signal on a large amount of background from light scattered mostly from the Raman fields but also from the MOT beams. I overcame the challenge of detecting a small signal above a large background by detecting the PMT signal with a lock-in amplifier (EG&G 5207 lock-in amplifier). I frequency modulated ('dithered') the detection laser while it was locked to the cooling transition and phase detected on this signal. This results in an amplitude-(not frequency-) modulated signal when scanning the Raman fields, and therefore the signal looks like a single peaked spectrum rather than a dispersive "Gaussian-derivative like" curve. I chose to frequency modulate the detection laser because it eliminates scatter from both the detection laser and Raman fields, and allows for a much shorter integration time for the signal than if I would have dithered the Raman fields [16].

3.5 Transverse Cooling

I attempted to control and reduce the atom beam divergence by adding a second optical molasses stage, a phenomenon described in Section 2.5. The second optical molasses beams were placed horizontally in the first window of the vacuum chamber and provide transverse cooling to the atom beam. This collimates the beam in the horizontal direction by reducing the horizontal component of the atoms' velocity. I took samples of the cooling and repump light, ensured linear polarization with $\lambda/4$ waveplates, overlapped them into one beam, split them into two beams with a polarizing beam splitter (PBS) and sent the resulting beams into the vacuum chamber from opposite sides, as shown in Figure 3.10, in order to produce the optical molasses. The cooling beam had an additional adjustable $\lambda/2$ waveplate and PBS to remove vertically polarized light as a way to to manually adjust the amount of cooling light in the optical molasses. The effects were measured by an infrared camera observing the width of the florescence in the detection beam and are discussed in Chapter 4.

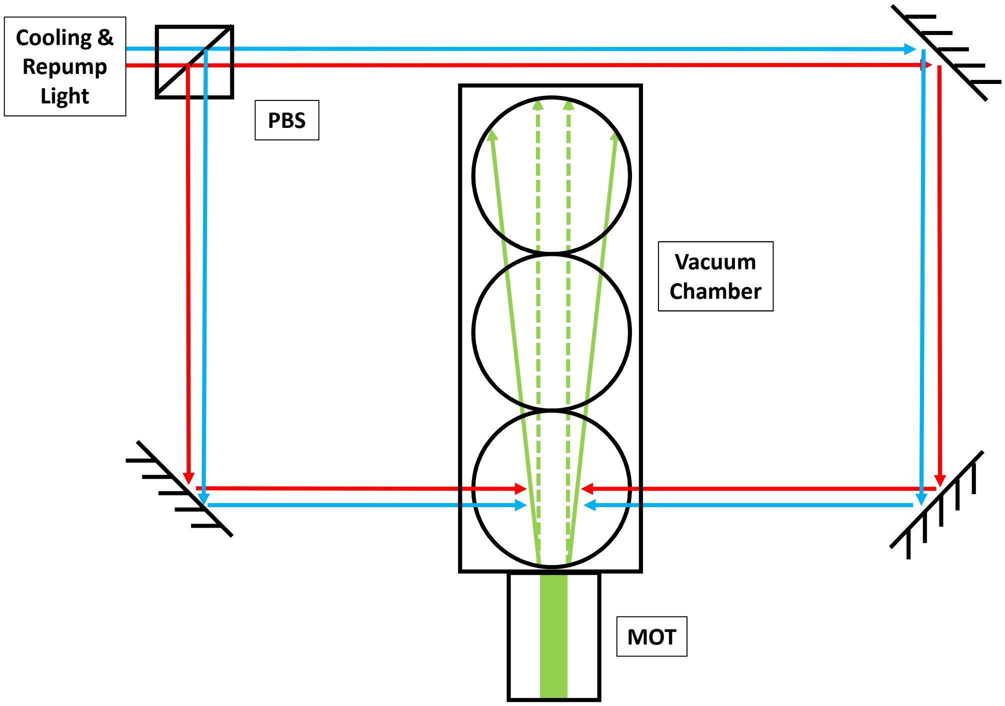

Figure 3.10. Simplified schematic of the optical molasses setup where the solid green lines are the current divergence of the atom beam, and the dashed lines are the projected divergence after transverse cooling occurs. (Optics for preparing polarization of cooling and repump light are not included)

3.6 Raman Setup

In Chapter 2, I introduced the theory underlying the Raman process. In this section, I detail how I created the laser that drives that process. I first took approximately 100mW of 780nm light from an amplifier and sent it through an AOM as shown in Figure 3.11. Building on the earlier description in Section 3.3.1, the AOM frequency shifts the light depending on the frequency of the RF source driving the modulator. My experiment only deals with the -1, 0, and +1 order outputs (light that is shifted to a lower frequency, at the same frequency, and increased in frequency, respectively), but other higher and lower orders were visible. I took the -1 order light (light that is shifted down in frequency) from the AOM and sent it to a fiber output. However, this process if far from efficient, and so I reflected the substantial amount of zeroth order light back through the AOM. The light is automatically phase matched to produce a +1 beam when the -1 beam is phase matched. The +1 order light was steered into a second fiber. These two fibers were then combined in a fiber beam combiner into a single physical laser beam with two frequency components, which I refer to as the Raman beam. Great care was also taken to ensure that one of the input lasers was made of horizontal linear light and the other of vertical. Although not perfect, the quality of the polarization was at least 90%. Selection rules, determined by atomic dipole moments and laser polarization, determined these choices in polarization [38].

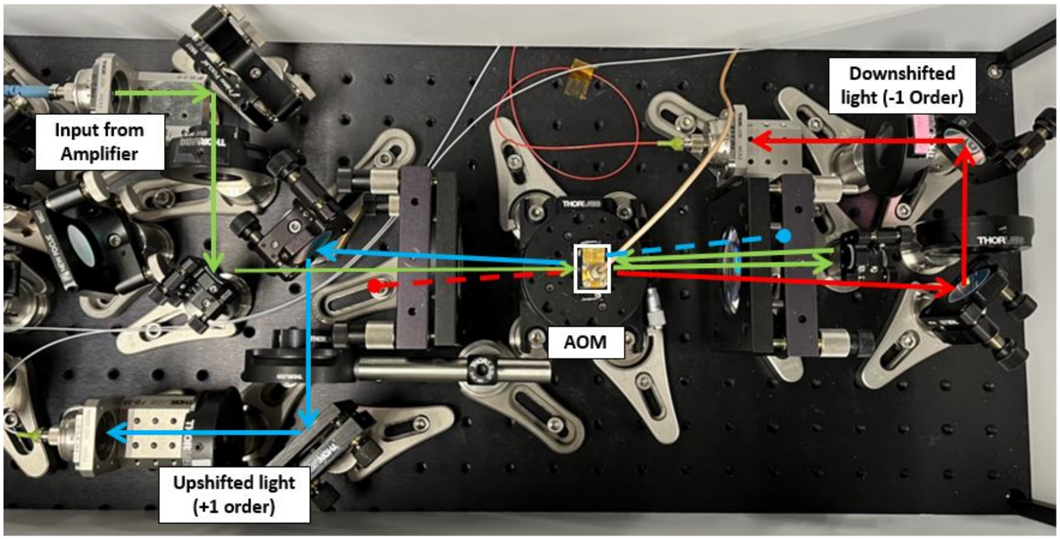

Figure 3.11. Image of the Raman setup I used including the optical paths. Red here represents the -1 order or lower frequency light emitted from the AOM, green is the zero order, and blue is the +1 order. I took the lower frequency of light from the first pass through the AOM and the higher frequency light reflected back through the AOM as the two frequencies for the Raman process.

Initially, I tried to generate a Raman spectrum using cylindrical lenses to shape the Raman beam into as close to a vertical rectangle as possible. While I was able to see a Raman spectrum, the laser beam profile still had a fair amount of Gaussian curvature, which largely explained the low signal, and I did not have much room to add the two additional beams to complete the interferometer. So I changed my configuration to a single large area beam created by allowing the laser output from the fiber to diverge to around a 4cm diameter beam before collimating it. I used 3D printed masks with one, two, or three slits to produce the right beam configuration to measure Raman, Ramsey interference, or Spin Echo interference respectively. For the co-propagating experiments, the beams were sent into the chamber and then incident on a dark beam-stop. For the Doppler sensitive counter-propagating Raman, I removed a beam stop from the back of the vacuum chamber and added quarter waveplates before and after the vacuum chamber, as well as a PBS and a mirror after. The PBS is used to remove one of the polarized beams of light to eliminate the possibility of driving the Raman transition with co-propagating fields from the retro-reflected Raman beams. I tested different slits of 1mm, 2mm, 3mm, and 4mm and found that the masks with width equal to 2mm produced the largest peak without significant broadening (from the small slits) or loss of signal from the large slits. I also characterized the Raman fields by taking images with a beam profiler, (see Figure 3.12), and found it be Gaussian in shape with half width 1/e value of σ = 11.2mm. These values were used in the simulations described at the end of Chapter 2.

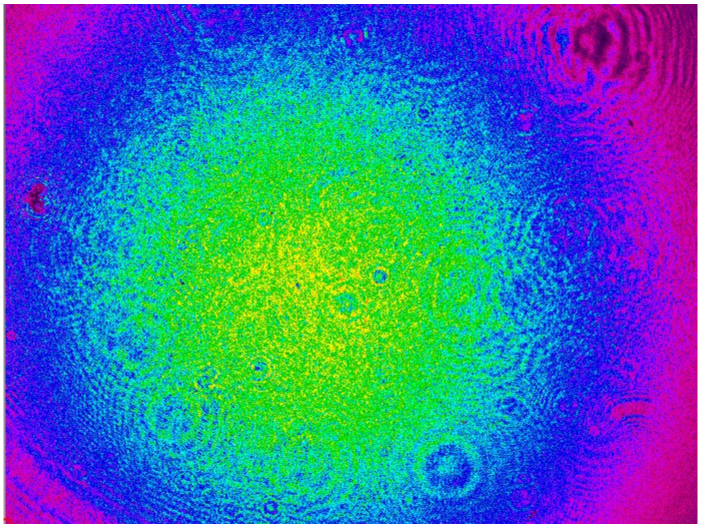

Figure 3.12. Photo of the Raman fields beam intensity profile with yellow being the highest intensity light.

3.7 Rabi Oscillations

Once the scheme to measure the Raman spectrum was established and working, I proceeded to the next step, which was to measure the Rabi oscillations. This step is integral in developing the interferometer because it provides us with the laser power levels needed to create the $\pi-$ pulse and $\pi/2-$ pulses. Rabi oscillations occur when the two Raman frequencies are tuned to be on two-photon resonance and the total power of the beams is varied (keeping the power ratio of the beams constant). I first attempted to do this by manually adjusting the Raman amplifier power over its full range and measuring the height above background of the clock transition (which is the $F = 2, m_F = 0$ to $F = 3, m_F = 0$ transition). This approach did not yield valuable results, likely due to the fact that changing the current to the amplifier change the amount of incoherent amplified stimulated emission which impacts the Raman spectrum. To avoid this problem, I added a voltage controlled attenuator (Mini-Circuits: ZX73-2500-S+40 dB Voltage Variable Attenuator) that I could ramp up and down using a function generator. I set the function generator for a 10 second ramp across the attenuator's full range with 99% symmetry (so I would only see results for high to low attenuation). I adjusted the frequency of the Raman fields so that they were in two-photon resonance with the atoms (e.g. at the peak of the Raman spectrum) and I recorded this signal along with the applied voltage to the attenuator and the signal from an optical power meter. The results of these measurements are discussed in Chapter 4. From these measurements, I could extract the proper power to provide π and $\pi/2$- pulses to maximize the contrast of the interferometer.

3.8 AC stark and Zeeman shifts

As already mentioned in Section 2.4, AC Stark and Zeeman shifts have deleterious effects on my measurements. In order to avoid these effects, I needed to "zero-out" the AC Stark shift and carefully characterize the Zeeman shift. The AC Stark shift depends on the difference in the power multiplied by the coupling constant for each transition. This value (and thus the shift) is only zero for all optical powers for a single ratio value of power between the two Raman fields. The experimental ratio value was found by switching from low to high power on the Raman fields, using the amplifier, and then adjusting the two different Raman fields frequencies' power until the the proper power ratio was found, and the shift zeroed-out. To characterize the Zeeman shift (which as discussed earlier is an energy level shift due to a magnetic field) I added a nominally uniform magnetic field to the vacuum chamber in the interferometry region. I accomplished this by placing two coils in a Helmholtz configuration and varying the current running through them. As discussed in Chapter 4, the full Raman spectrum consists of 11 peaks numbered -5 to 5 with 0 being the clock transition. The magnetic field not only shifts the location of the peaks, but also the amplitude of the peak [39], [40]. Using this method, I determined the current needed to maximize the clock transition peak and well separate all the peaks in the spectrum (0.5 Amps). Results of Zeeman testing are shown in Figure 3.13, where the more positive current corresponds with increased amplitude and separation in even Raman peaks.

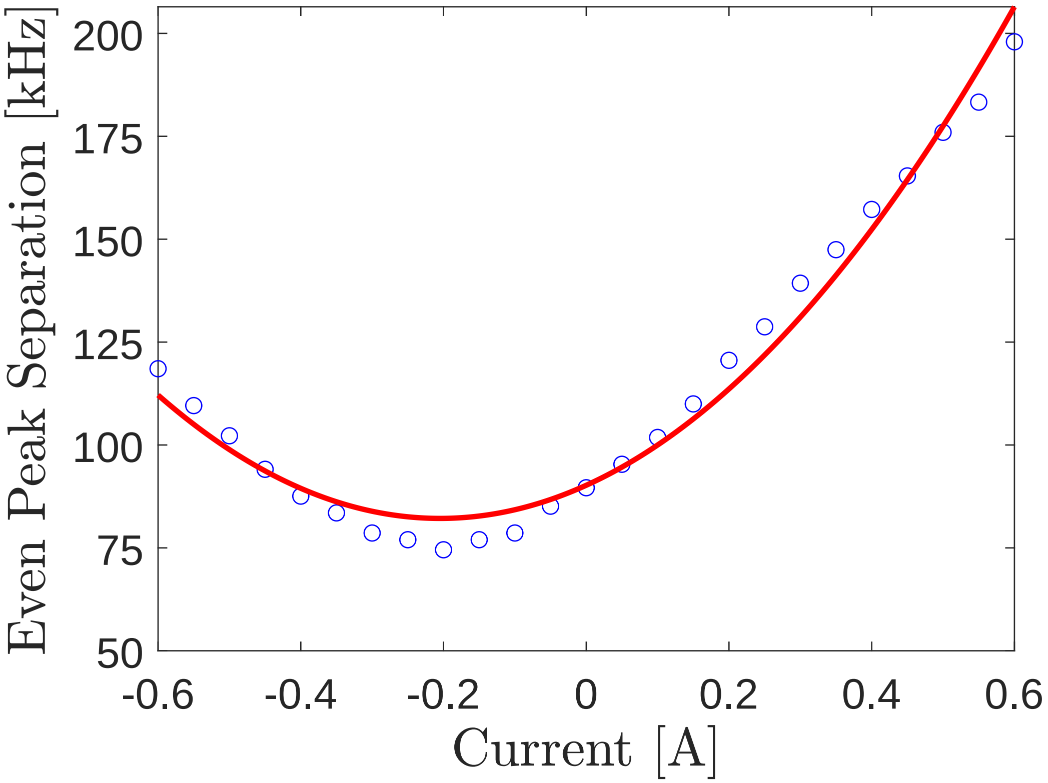

Figure 3.13. Peak to peak separation of the clock and -2 Raman transition from Zeeman shift due to magnetic field supplied by coils. The red line is quadratic curve fit.

3.9 Interferometer

The configuration of optics used for the interferometer is shown in Figure 3.14. This displays the full counter-propagating setup and works as follows. The light exits the fiber-coupler and diverges until the collimating lens. The light then then passes through a $\lambda/4$ waveplate (to convert the light into circularly polarized light to be able to obey selection rules) and through the masks with slits for the different configurations, and finally into the vacuum chamber. After interacting with the atom beam and exiting the vacuum chamber, the light passes through a second $\lambda/4$ waveplate (to convert the light back into linear polarization), a PBS (which rejects one of the laser frequencies), and then onto the retro-reflecting mirror, which directs the light back onto the atoms. In order to switch to the co-propagating geometry, I removed the first $\lambda/4$ waveplate and place a beam block on the back of the vacuum chamber. Figure 3.15 shows a mask with spin echo configuration.

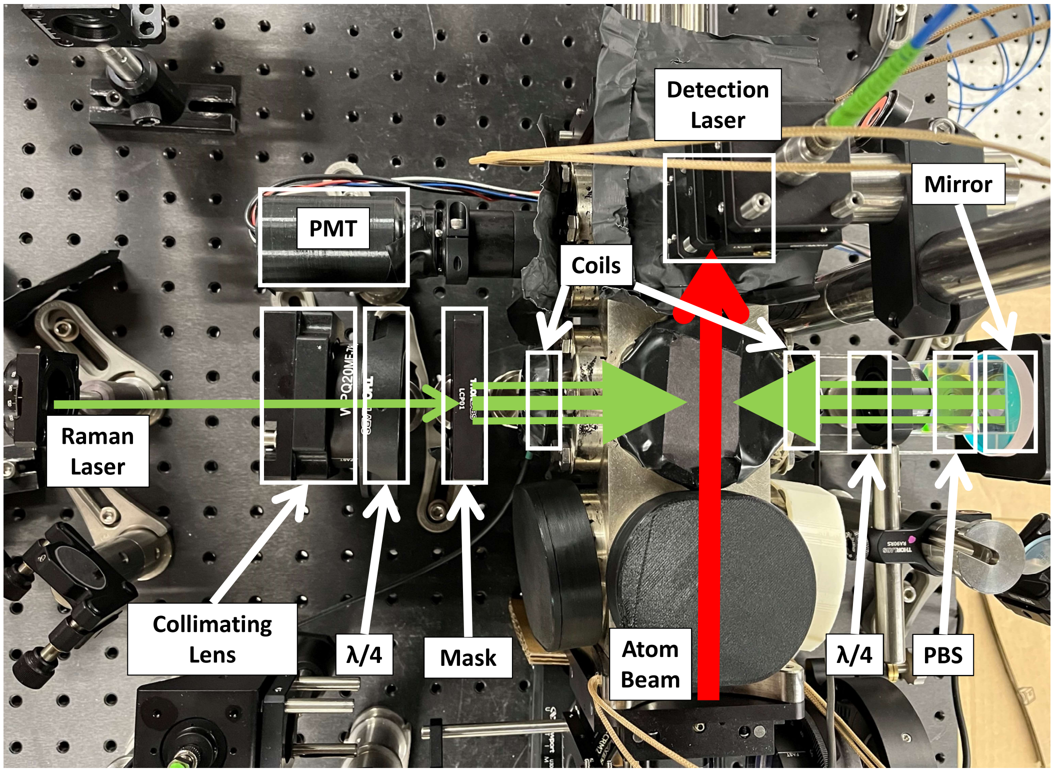

Figure 3.14. Schematic of optics and apparatus for counter-propagating configuration.

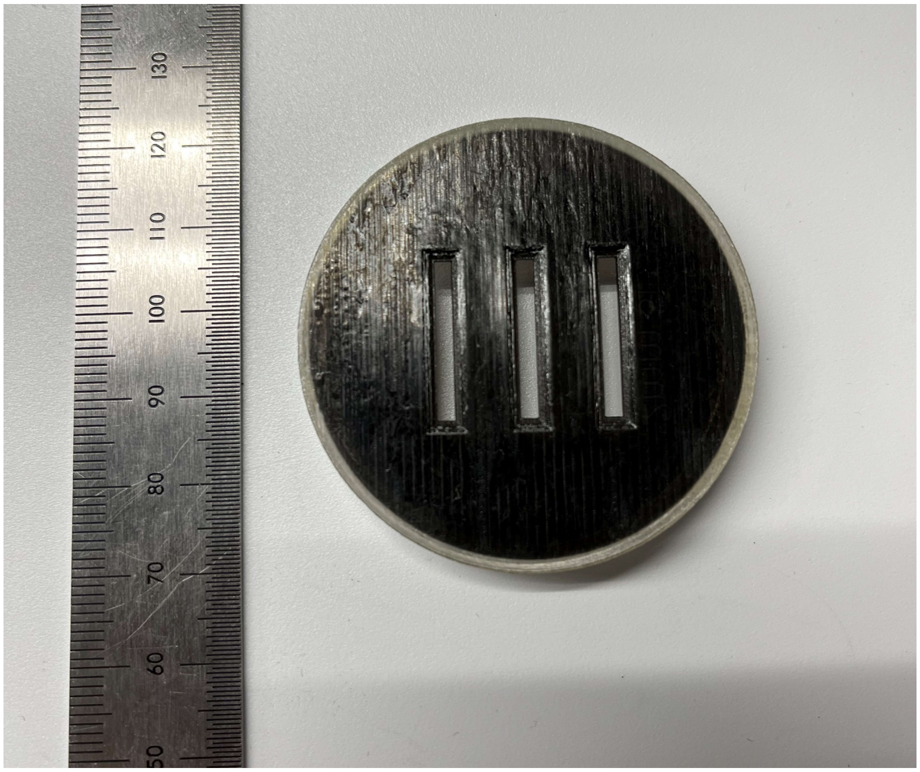

Figure 3.15. Image of the 3D printed masks used for spin echo interference with ruler for scale.

CHAPTER 4:
Results

In the previous chapters, I outlined the theory behind the experiments and described the apparatus used to make the measurements. In this chapter, I present the results of those measurements.

4.1 Optical Molasses

In Figures 4.1, 4.2, and 4.3, I demonstrate that the optical molasses I prepared, described in Section 3.5, was able to provide a useful amount of transverse cooling. It was employed to narrow the atom beam divergence, with the specific intent to improve the signal from the counter-propagating configuration. The optical molasses is a function of the laser cooling power. Rather than control the power through the current of the tapered amplified (with the problems of amplified stimulated emission described before), I employed a common optics technique to more finely control the laser power. As described in Section 3.5, I passed the cooling light (which was linearly polarized), through a $\lambda/2$ plate and then a polarizing beam splitter. Figure 4.1 shows the measured laser cooling power as a function of the wave plate angle (ϕ). Figure 4.2 (top) shows the results of the images of the atomic beam as a function of the wave plate angle and hence the cooling power. Figure 4.2 (bottom) shows the results of plotting a vertical "slice" taken through the image along the brightest part of the beam. We can see that for certain angles (specifically near to 45° degrees) the resulting peaked function is taller and narrower. This result indicates that the atomic beam has spread out less (narrower slice) and has more atoms in the center (taller peak). These slices were then fit with a Lorentzian function and the peak value and linewidth were extracted. The linewidth is measured as the halfwidth of the peak at half of its maximum amplitude. This is a common metric for linewidth referred to as half width at half maximum (HWHM). These two specific parameters are plotted in Figure 4.3, where we again can see that around $\phi = 45°$, the beam is narrowed (smaller HWHM) and has more atoms in the center (higher peak atom number). Unfortunately, due to physical spatial constants with the vacuum system, I could not employ the optical molasses beams, the optical pumping beams, the Raman beams and the detection beams required for the full experiment. The interferometer also depends on atomic coherence, which can be destroyed when atoms scatter near-resonant light. This was a concern because the optical molasses that employed near resonant light was very close to the location of the interferometer. As a result, I decided not to include the optical molasses set up in the rest of the experiments. However, I have conclusively shown that this technique is a viable way of narrowing the atomic divergence and can be useful in future experiments.

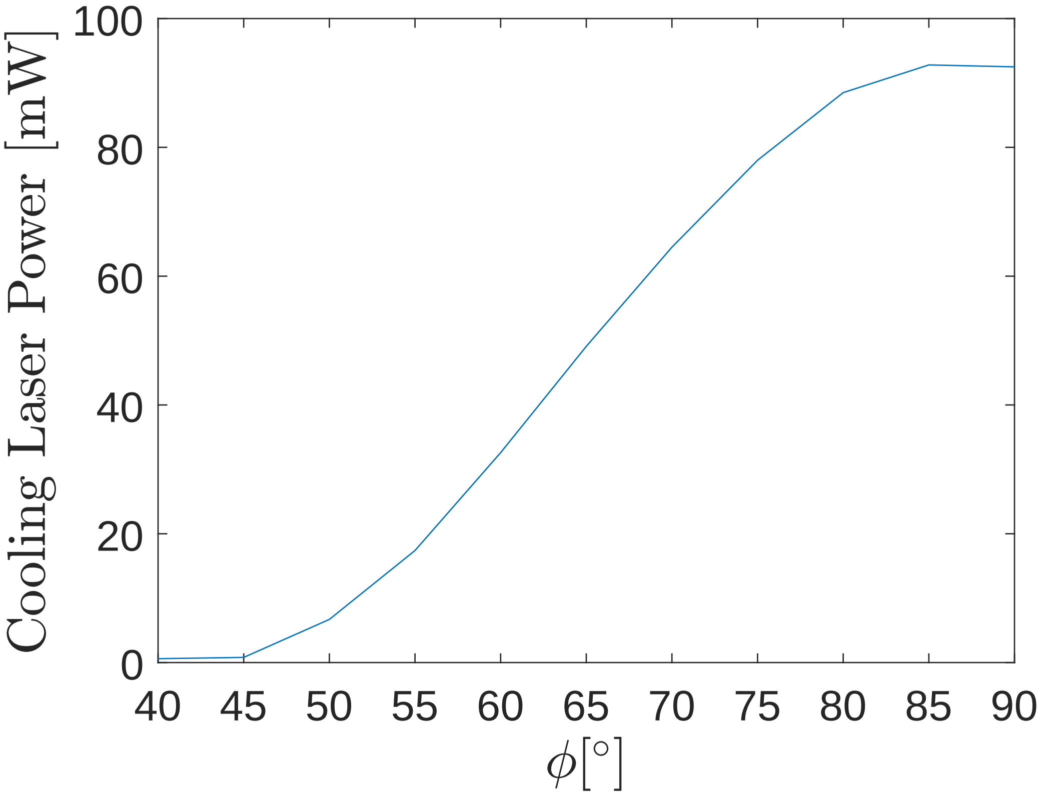

Figure 4.1. Plot of how the cooling laser power varies over $\lambda/2$ waveplate angles (ϕ), going from minimum to peak power across polarizations.

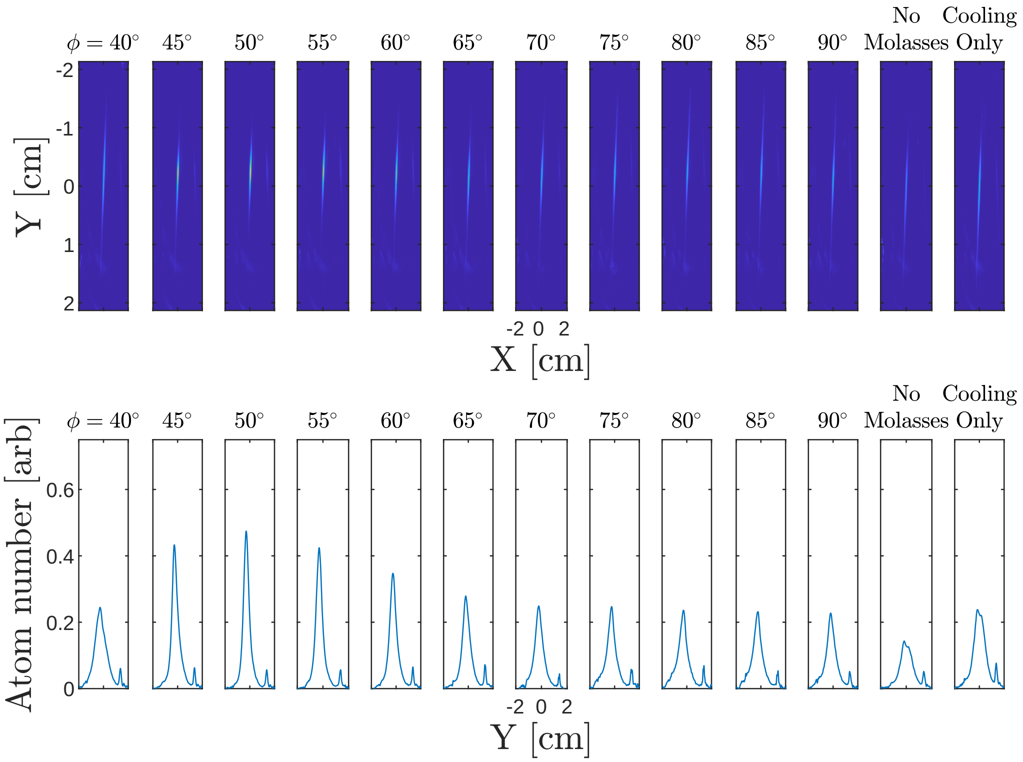

Figure 4.2. Plot of transverse cooling effects across different polarization settings on a $\lambda/2$ waveplate. We can see successful transverse cooling at smaller angles with the higher atom counts and across most angles as thinner line widths compared to the two reference peaks on the right.

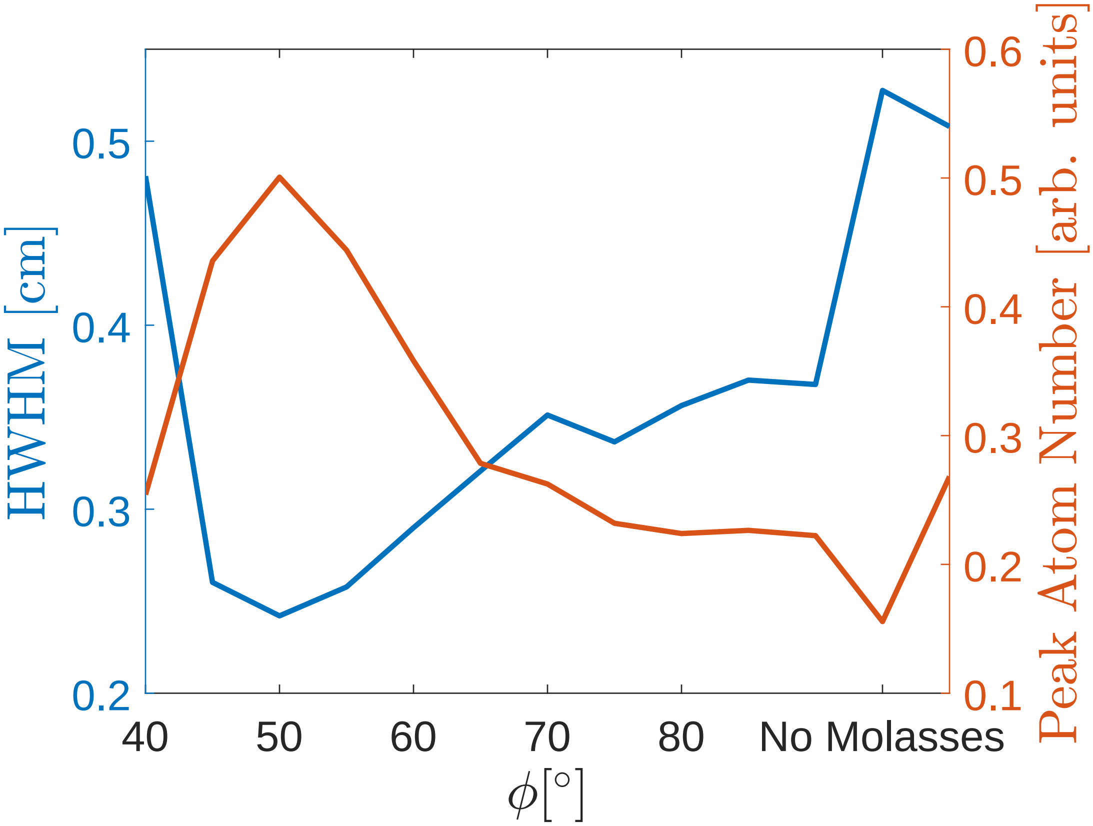

Figure 4.3. Plot of linewidth as HWHM (left axis), and peak amplitude (right axis) versus ϕ. We can again see very successful transverse cooling at smaller angles with higher peak atoms and thinner line widths as the atoms are kept from diverging.

4.2 Raman Spectroscopy

Despite not being able to implement a method to reduce the atom beam divergence, our simulations showed that the atomic divergence will impact the counter-propagating experiments, but will not completely wash out the spectra I will be measuring. Once I had set up the dual frequency Raman laser described in Section 3.6, I performed experiments in the co- and counter-propagating configurations. Figure 4.4 shows the complete Raman spectrum in the co-propagating configuration. As discussed in [39], [40], when the magnetic field and the Raman fields polarizations are left arbitrary with respect to each other, up to 11 peaks are expected due to the selection rules between transitions with different magnetic states.

This is shown in Figure 4.4, taken in the co-propagating geometry.

Figure 4.5 shows an important progression and a significant step in the demonstration of a full inertial sensor. I first note that if I simply pass the Raman fields through the atomic beam and then retroreflect the beams, I will NOT be measuring a Raman spectrum in a counter-propagating geometry for three reasons. First, the spectrum from the co-propagating geometry will still be present, as will the same for the two retro-reflected beams that are also now co-propagating. Secondly, depending on the orientation of the laser fields with respect to the magnetic field, the relative polarization of one beam in the forward direction may not be the right one to match up with the counter-propagating one. Finally, if the two polarizations do happen to match, there will be *two* combinations of Raman fields with opposite Doppler shifts. For all three reasons, it is important to eliminate driving a Raman resonance in the co-propagating geometry and drive only one in the counter-propagating geometry. The results of this progression show how the peak disappears when a $\lambda/4$ waveplate is added to the co-propagating setup (which causes the two co-propagating fields to have the "wrong" polarization to drive a Raman resonance) and how the peak reappears when the beam block is removed to allow counter-propagating light back in. The combination of an extra $\lambda/4$ waveplate and PBS ensures that only one frequency is retroreflected back into the chamber, eliminating the second possible Raman resonance in the counter-propagating geometry. The results of these measurements demonstrate that what we are seeing is actually a Raman spectrum from counter-propagating fields. The $\approx$ 1/3 drop in amplitude between co-propagating and counter-propagating Raman should be noted. As predicted in Section 2.9, this is a result of the effect of atom beam divergence and transverse velocity averaging. All the following scans used a 2mm mask slit width.

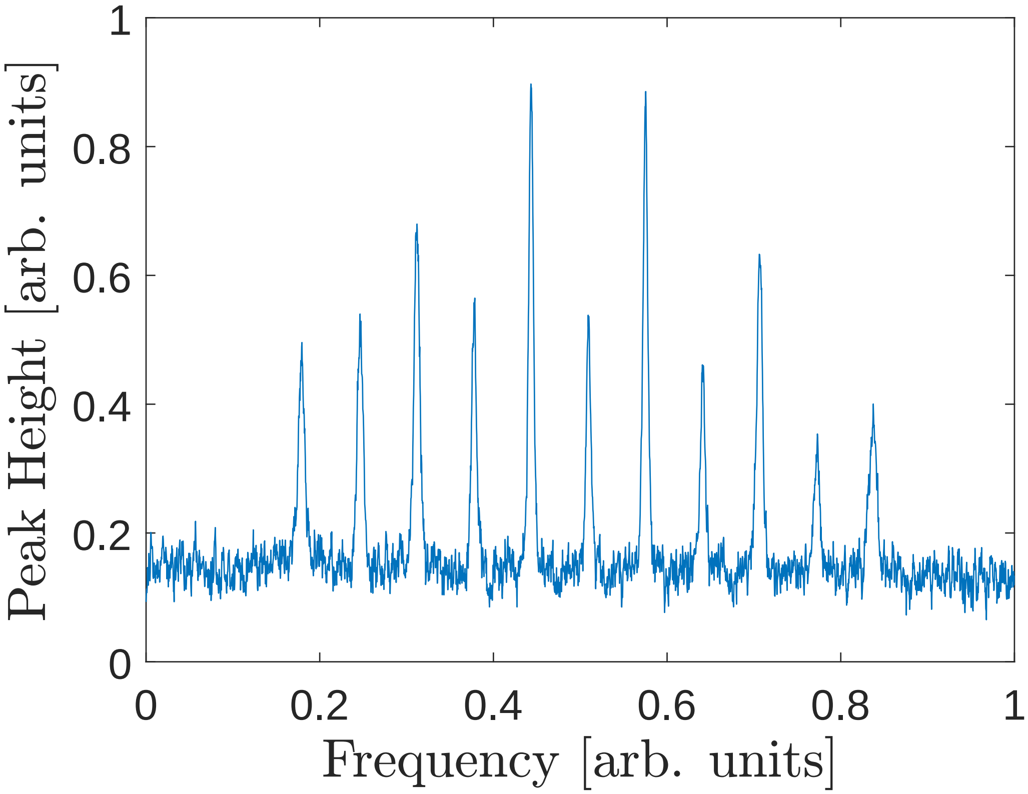

Figure 4.4. Scan of the full Raman spectrum with 11 peaks at different frequencies. These peaks correspond to the 11 different transitions of the $F = 2$ to $F' = 3$ hyperfine magnetic sub-levels resulting from the nuclear magnetic moment.

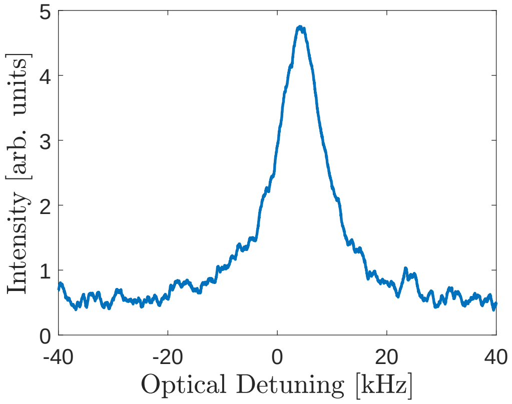

(a) Co-propagating Raman

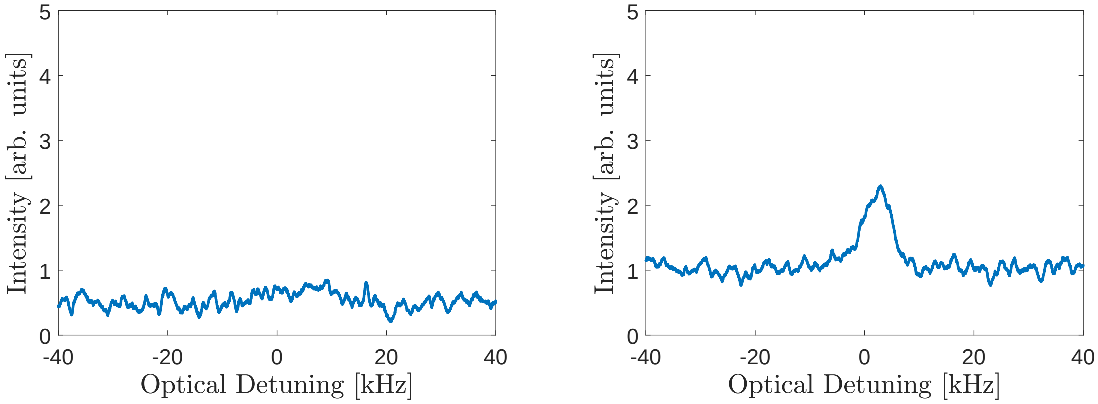

(b) Dead Raman

(c) Counter-propagating Raman

Figure 4.5. Figure (a) shows co-propagating Raman, figure (b) depicts a loss of the signal resulting from adding a $\lambda/4$ waveplate to circularize the polarization, and figure (c) is the reappearance of Raman in the counter-propagating configuration once I removed the beam block.

Once I was able to produce clear Raman spectra, I needed to determine at what power levels the π and $\pi/2-$ pulses occur. As mentioned in Section 2.2.1, this determination is made by measuring Rabi oscillations. I begin by tuning the Raman fields onto resonance of the clock transition and then fixing the detuning so that the Raman fields are driving the resonance at the peak. I then use a variable attenuator to ramp the power of the Raman laser from low to high power. This will cause the laser to increase in intensity across a large enough range to see the first Rabi oscillation. The resultant scan, as shown in Figure

4.6 depicts the first Rabi peak and subsequent dampening along with a trace of the voltage ramp applied to the attenuator. To determine where a $\pi-$ pulse occurs I match the peak of the first Rabi oscillation to the corresponding voltage on the attenuator. A $\pi/2$ pulse is determined by finding the halfway point in terms of height on the first Rabi oscillation and its corresponding attenuator voltage. These voltages are then input directly to the attenuator and then measurements of the laser power are taken on the back side of the vacuum chamber for π and $\pi/2-$ pulses to be used in determining proper power levels for the Ramsey and spin echo interference experiments.

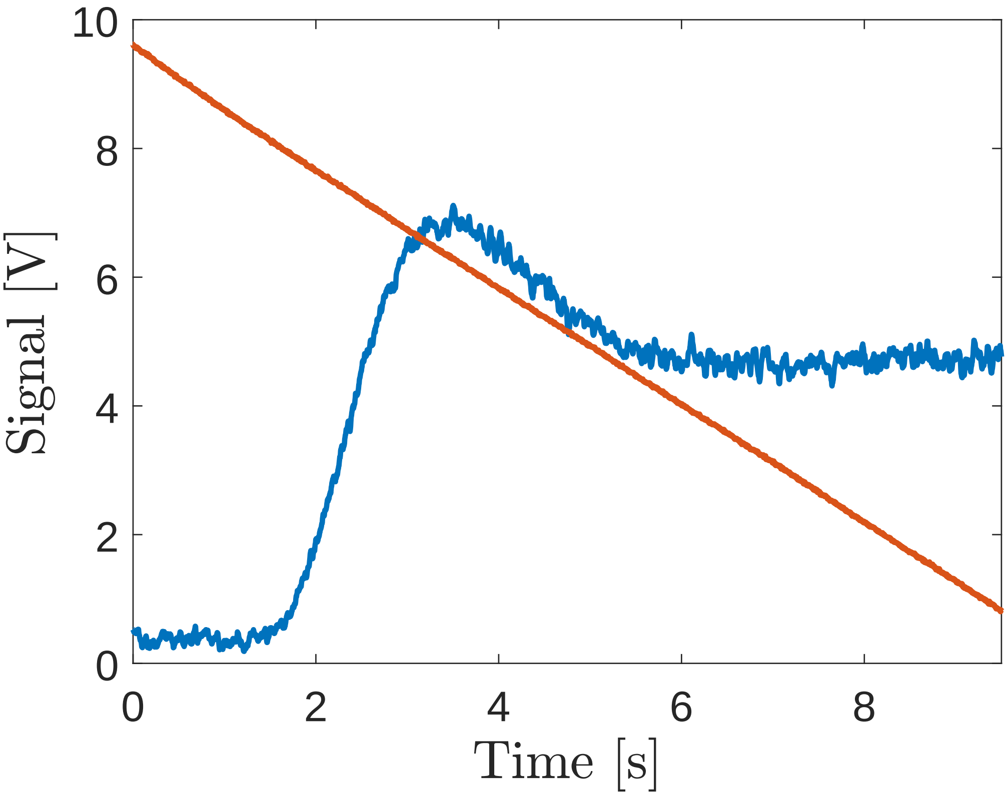

Figure 4.6. Scan containing Rabi oscillations (blue) and voltage level on variable attenuator (red).

I also sought to characterize the linewidth of the clock transition over various scan times. All transitions have a fundamental linewidth. For example, linewidths of single photon transitions are determined by the reciprocal of the excited state lifetime. For Raman transitions, the linewidth is determined by the time the atom spends in the laser fields. However, these statements are only true when the measurement time is much longer than any process in the experiment. If the scan of the Raman fields' frequency is too fast, you will observe a peak that is too wide (measurement broadening) and if you scan too slow, the measurements can take an inefficient amount of time. I characterized the linewidth by fitting the Raman peaks to a Lorentzian function with a parameter β corresponding to the HWHM. I measured the spectrum for many different ramp dwell times (time spent at each step in the scan generated from a digital signal synthesizer), and extracting the parameter β each time. I then fit the results to a decaying exponential and chose an arbitrary cut off of 3 times the time constant, τ as the minimum ramp dwell time. 3τ is the value at which the linewdith is within 95% of the actual linewidth as compared to 86.5% for 2τ. I used 40 μs for most scans just to be on the safe side.

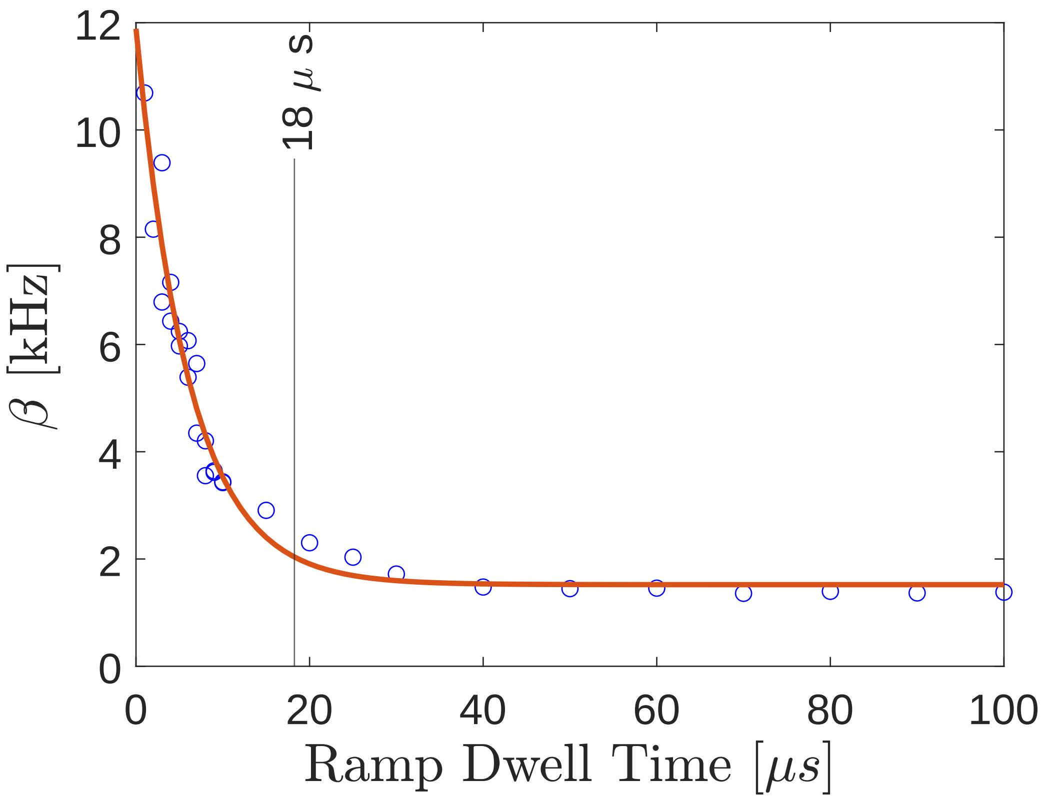

Figure 4.7. HWHM values over multiple ramp dwell times with $18\mu s \approx 3\tau$.

4.3 Co- and Counter-Propagating Ramsey Interference

Once I was able to achieve and characterize co-propagating and counter-propagating Raman, I then moved to a Ramsey configuration. Figure 4.8 displays the resultant scans of Ramsey interference followed by the measurement of counter-propagating Rabi oscillations used to determine $\pi/2-$ pulse power levels. Similar to Raman, counter-propagating Ramsey is noticeably weaker than in the co-propagating configuration.

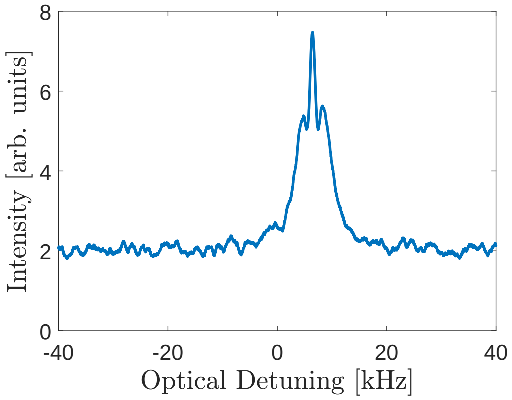

(a) Co-propagating Ramsey

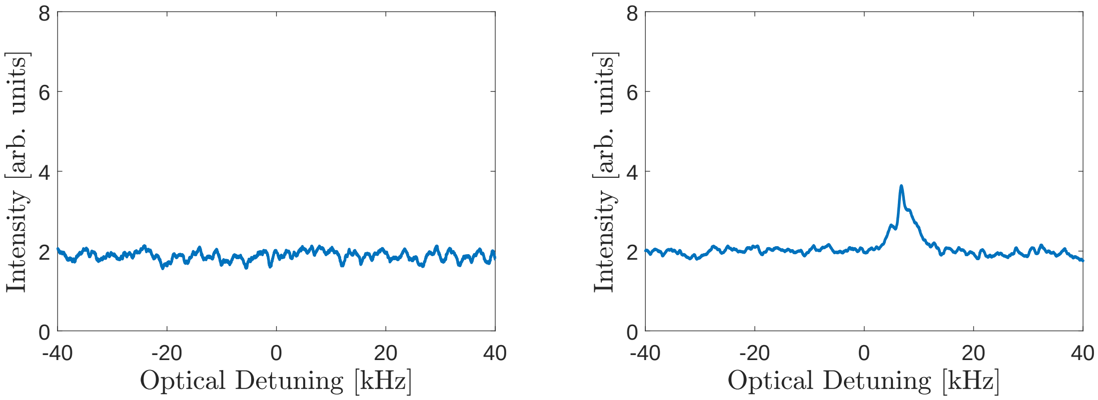

(b) Dead Ramsey

(c) Counter-propagating Ramsey

Figure 4.8. Figure (a) shows co-propagating Ramsey, figure (b) depicts a loss of signal resulting from adding a $\lambda/4$ waveplate to circularize the polarization, and figure (c) is the reappearance of Ramsey in the counter-propagating configuration once I removed the beam block. Scans were taken using 4x averaging.

Once I was assured that I was seeing counter-propagating Ramsey I then drove Rabi oscillations as shown in Figure 4.9. This was to determine the π and $\pi/2-$ pulse conditions which are required to maximize the contrast in the Ramsey and spin echo experiments. Figure 4.10 depicts a typical Ramsey interference spectrum, taken under the conditions of π and $\pi/2$ extracted from the Rabi characterization.

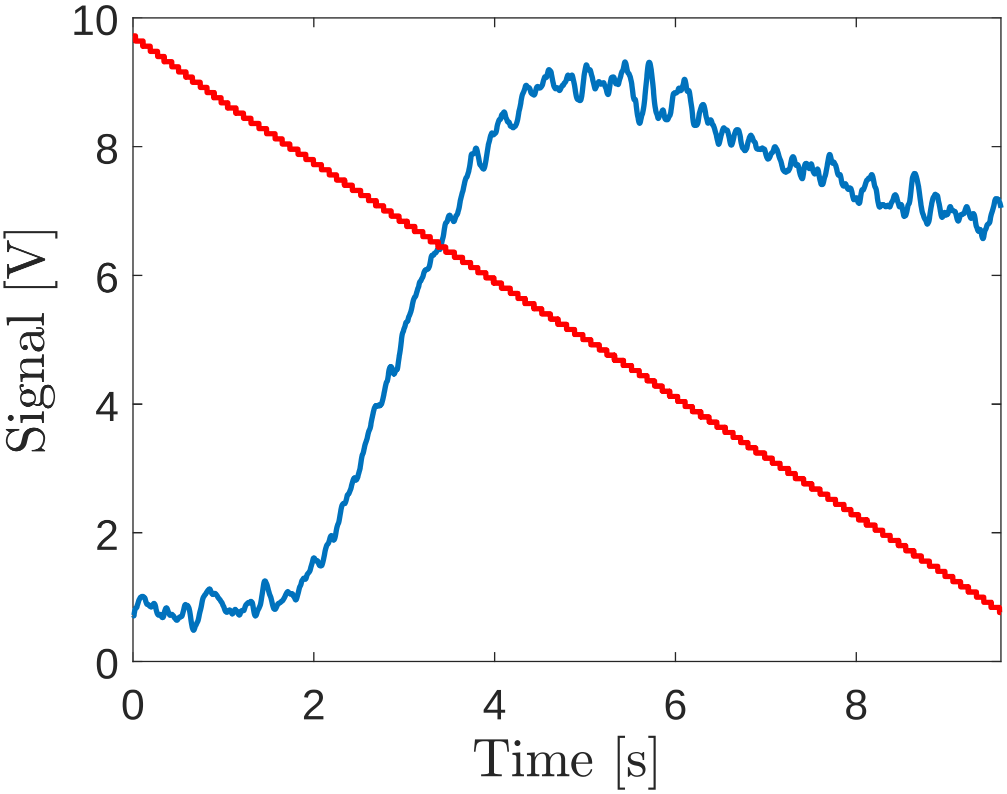

Figure 4.9. A smoothed curve of counter-propagating Rabi oscillations (blue) and voltage level on variable attenuator (red).

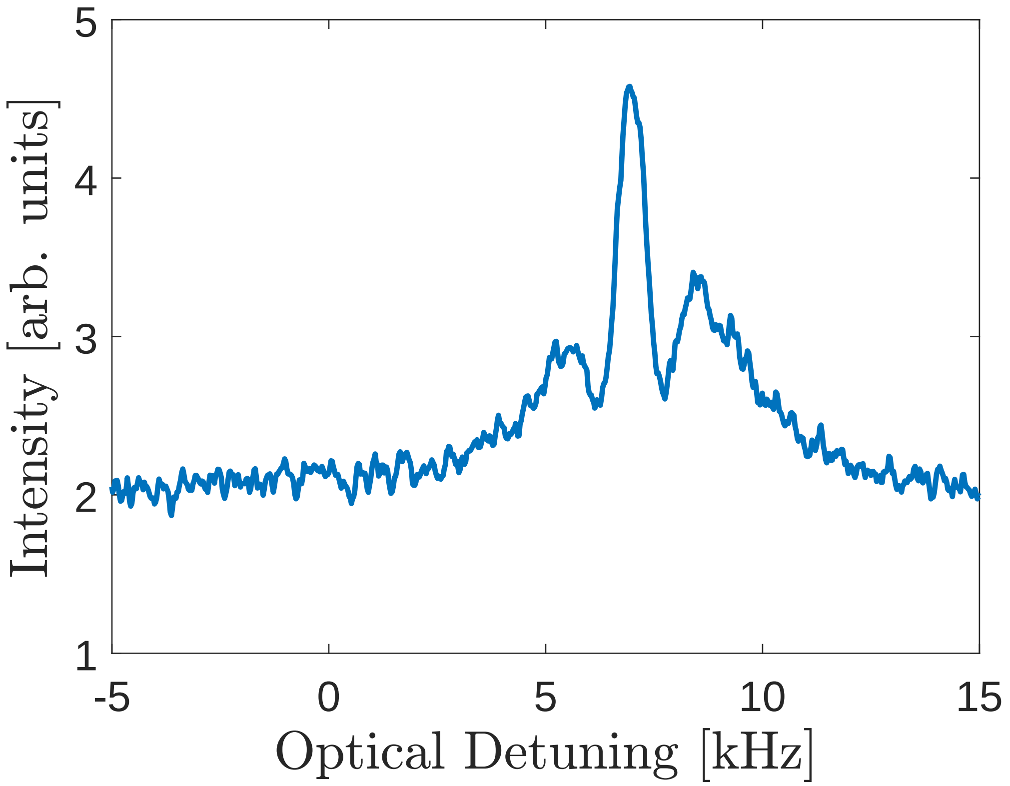

Figure 4.10. Counter-propagating Ramsey interference averaged 8x for a 400 μs ramp dwell time.

4.4 Scan Time

The last experimental parameter I characterized is the ramp dwell time for the Raman fields when measuring the Ramsey and spin echo spectra. This parameter is the same as the one measured in the Raman spectra section. However, because the Ramsey and spin echo experiments have finer details, the ramp dwell time is expected to be different. The total scan time is calculated from the number of steps in the scan (generated from a digital signal synthesizer as previously noted) multiplied by the dwell time at each step (ramp dwell time). If the ramp dwell time is too fast, it will average out fine details and not provide the contrast I need. Conversely, if the ramp dwell time is too slow I was being inefficient with our scans. Contrast, as defined by Equation 2.11, was calculated for both the center peak and the secondary peaks of the interference spectra. I performed experiments for co-propagating and counter-propagating Ramsey interference over increasing ramp dwell times examining how the contrast changed. Figure 4.11 shows the results of these contrast measurements. I note that the contrast is on the same order as the contrast from the simulated results shown in Figure 2.7, particularly for the counter-propagating setup. This would suggest a system performing at its fundamental limit.

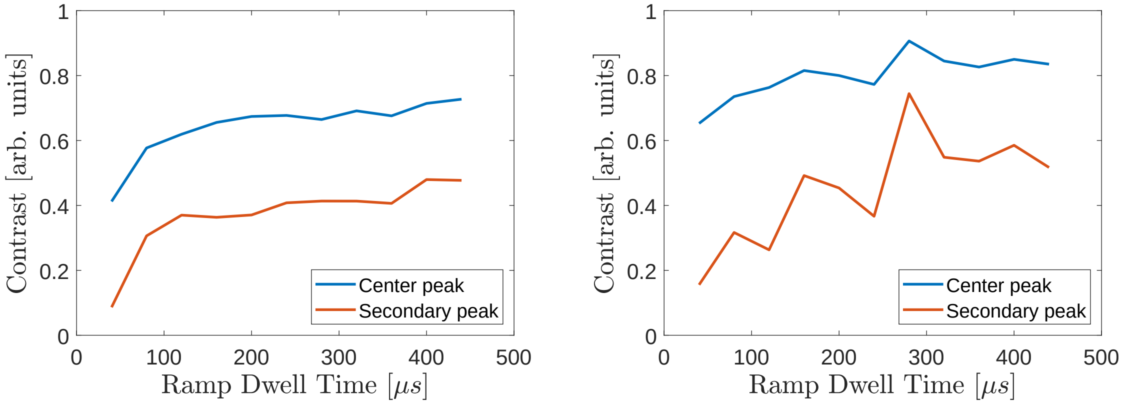

(a) Co-Propagating Ramsey contrast

(b) Counter-Propagating Ramsey contrast

Figure 4.11. Figure (a) displays the co-propagating Ramsey contrast values vs ramp dwell time for the center peak and secondary peak. Figure (b) displays the same values for counter-propagating Ramsey. A slit spacing of 8mm was used.

I then fit the results from the center peak contrast to a charging exponential equation to determine the optimal ramp dwell time shown in Figure 4.12. I looked at an arbitrary cut off of 3τ, similar to the linewidth analysis in Section 4.2. This provided us with a value of $\approx 200\mu$s as that would provided roughly 90% of full contrast for counter-propagating configurations.

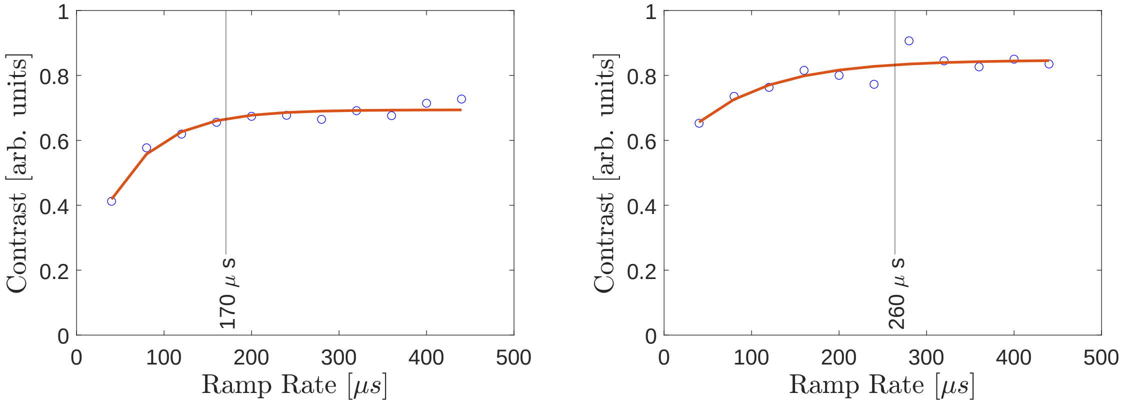

(a) Ramp dwell time fit for Co- Ramsey (b) Ramp dwell time fit for Counter- Ramsey

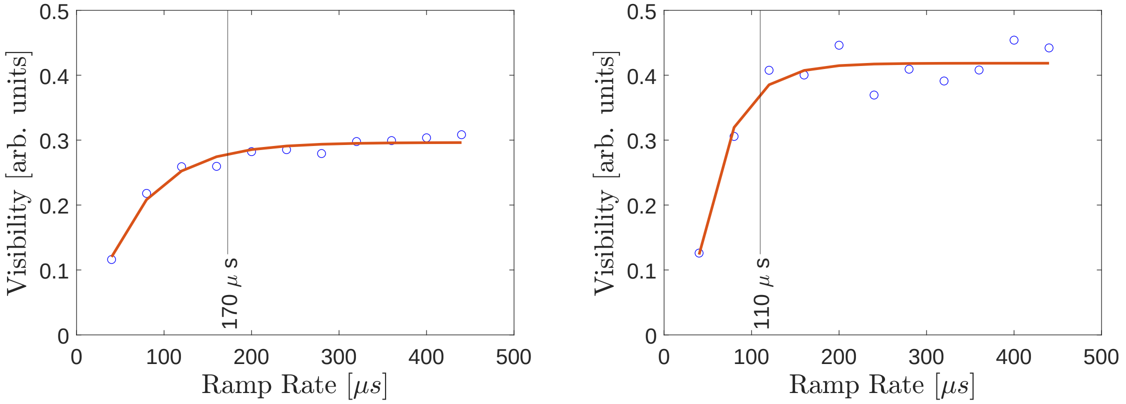

(c) Visibility fit for Co- Ramsey (d) Visibility fit for Counter- Ramsey

Figure 4.12. Figure (a) is the curve fit for co-propagating Ramsey showing an optimal ramp dwell time of 170μs. Figure (b) is the curve fit for counter-propagating Ramsey showing an optimal ramp dwell time of 260μs. Figures (c) and (d) are for the same data but used a modified Gaussian fit of the Ramsey spectra and used a visibility coefficient instead of the manually calculated contrast. The change in scale between the rows is due to the different fit parameters being graphed. A simulated slit spacing of 8mm was used.

As can be seen in Figure 4.13, the Gaussian fits modified to include an interference envelope are not ideal. This is due partially to the asymmetry of the Ramsey peaks, leading to lower fidelity in using the 110μs ramp dwell time. Therefore, I elected to use a ramp dwell time of 200μs.

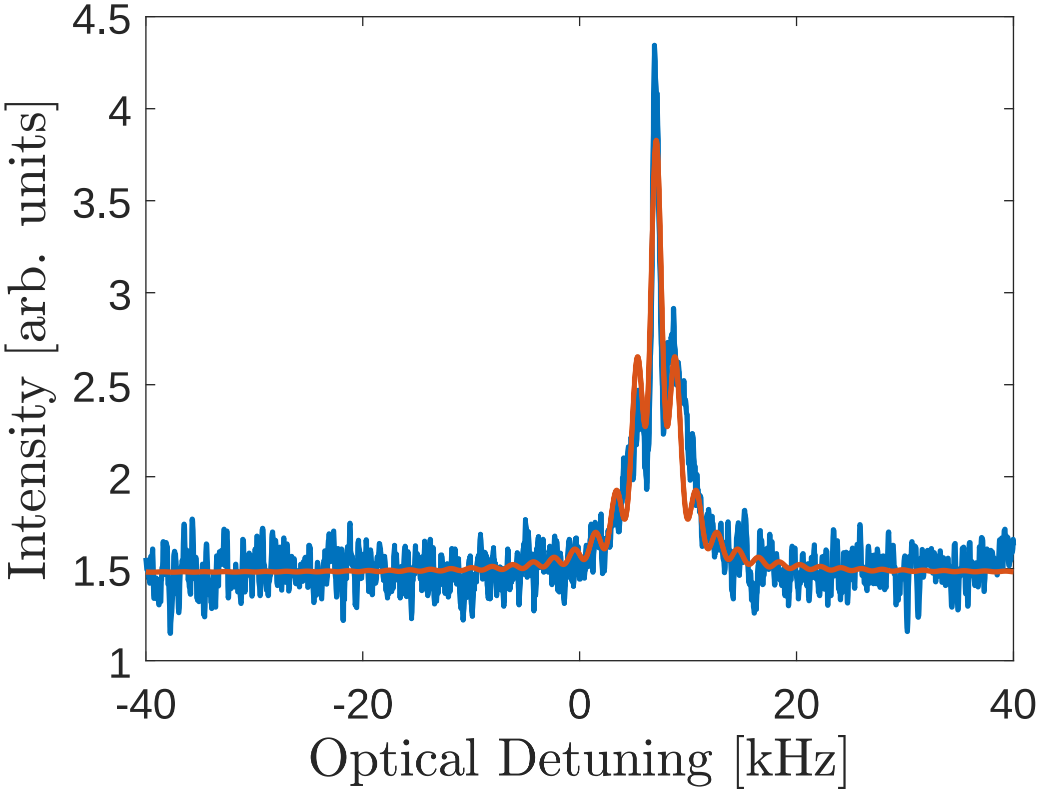

Figure 4.13. Example of poor modified Gaussian fit to a Ramsey fringe. Note the lower center peak amplitude and misaligned secondary peaks. Data is for a ramp dwell time of 320μs.

4.5 Spin Echo Interference

I now have completed all the necessary steps in preparation for utilizing the full spin echo configuration. I had a custom mask printed based on the dimensions supplied in Section 2.9.3 (see Figure 3.15). The results based on pulses configured from Rabi oscillations are in Figure 4.14 with a zoomed-in interference fringe in Figure 4.15.

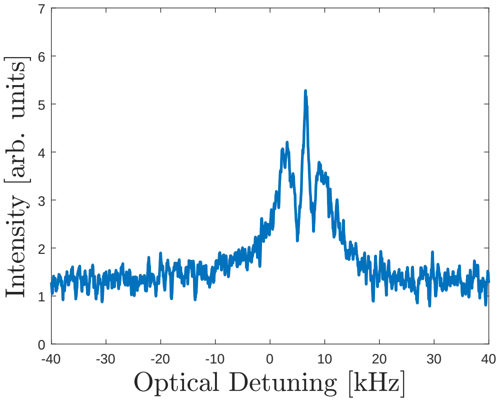

(a) Co-propagating SE

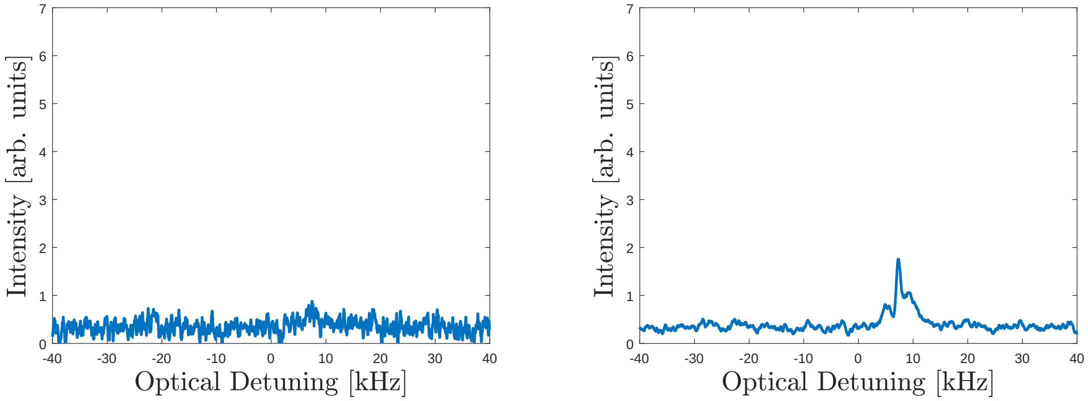

(b) Dead SE

(c) Counter-propagating SE

Figure 4.14. Figure (a) shows co-propagating spin echo, figure (b) depicts a loss of signal resulting from adding a $\lambda/4$ waveplate to circularize the polarization, and figure (c) is the reappearance of spin echo in the counter-propagating configuration once I removed the beam block. Scans were taken using 4x averaging.

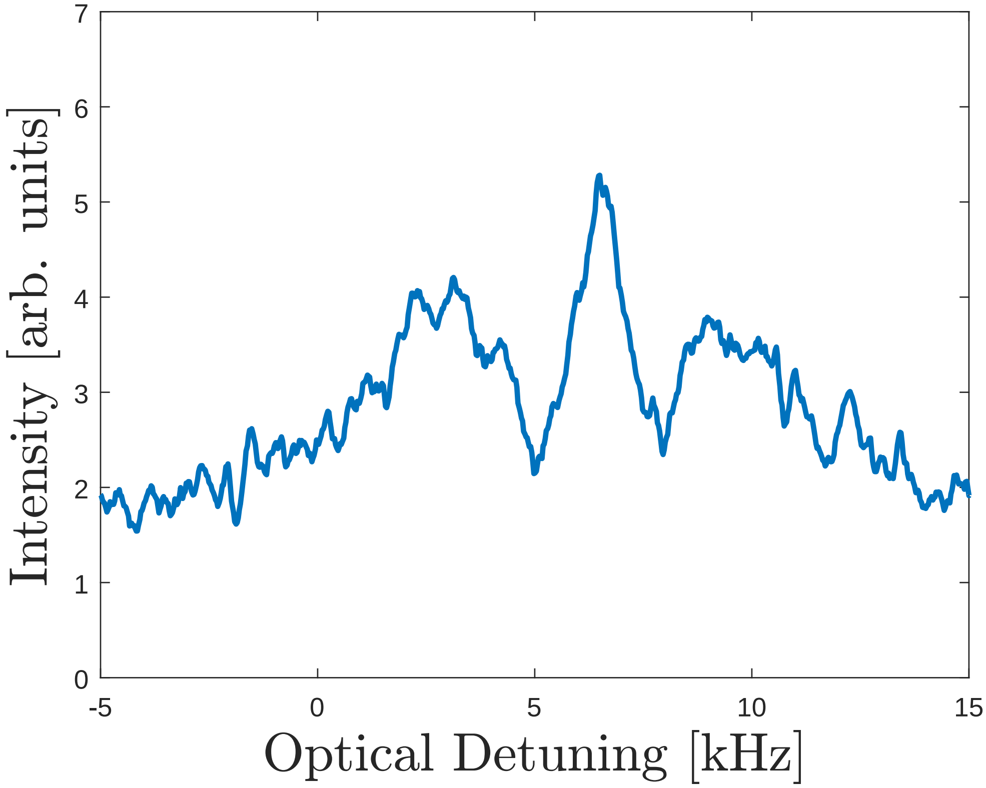

Figure 4.15. Co-propagating spin echo interference averaged 8x for a 400 μs ramp dwell time.

THIS PAGE INTENTIONALLY LEFT BLANK

CHAPTER 5:
Conclusions

In this thesis, I covered the theory, setup and characterization, and experimental results of a continuous atom beam interferometer. In Chapter 2, I discussed the theory behind atom interferometers, cooling and trapping atoms, and how the atoms optics are created through the Raman process. I discussed simulations that included the effects of atom beam divergence and velocity averaging. The results of the simulations showed that the co-propagating configurations of Raman, Ramsey, and spin echo are not affected much by the divergence of the atom beam, but are affected by the velocity averaging. The simulations also revealed that in the counter-propagating configurations both atom beam divergence and velocity averaging significantly affect the interference spectra.

In Chapter 3, I discussed the design and optimization of the apparatus, the characterization of the atom beam, and how the Raman fields were prepared for interferometry. These topics showed how I improved the SNR of the detection laser, how I measured and calculated the divergence and most probable velocity of the atoms, and how I prepared the Raman fields and associated spectra for interferometry. I also discussed the design of an optical molasses to potentially reduce atomic beam divergence.

In Chapter 4, I presented the results of the experiments. I showed how the addition of a second optical molasses could reduce the divergence of the atom beam and potentially increase the amplitude of counter-propagating interference patterns. I demonstrated how I determined the optimal scan parameters for producing results with the greatest contrast in the most efficient amount of time. Lastly, I demonstrated the potential for interference measurements with the current setup.

Although not discussed in detail, significant work was done to better stabilize the system for long term measurements, as was required by the experiments I discussed. The locking frequency of several lasers was shifted to more stable locations with the addition of single and dual pass AOMs (discussed in Section 3.3.1. The Raman fields were low on power until an amplifier was added. The use of masks and a single large area Raman field setup, instead of pulsed or multiple lasers, also provided more consistent results.

Due to their setups, the laser preparations are well characterized and found to be good candidates for scaling down in size in future designs. The vacuum chamber is prepared to add a second atom beam, but needs more development for inclusion of the quantum state preparation and detection beams. Also, adding two more sets of windows would provide the space for a full dual atom beam interferometer/gyroscope. While I did not meet the initial goal of taking inertial measurements, that experiment is fully prepared to begin with minor adjustments.

Future experiments should replicate our counter-propagating results adding the second atomic beam and attempt to measure the earth's rotation. The apparatus has also been proposed to be placed on a rotation stage to measure imparted rotations as a prelude to measuring the earths rotation [16]. Further work will also need to address the divergence of the atom beam, and the long terms stability of the apparatus. There is also room for improving the setup for inertial measurements beyond the earth via a rotation stage that had previously been proposed.

List of References

[1] "Navigation (NN) and Seamanship (NS) course information," USNA [Online]. Available: https://www.usna.edu/Academics/Majors-and-Courses/course-description/NS.php

[2] M. S. Grewal, *Global Navigation Satellite Systems, Inertial Navigation, and Integration*, 4th ed. Hoboken, New Jersey: John Wiley & Sons, Inc., 2020. Publication Title: Global navigation satellite systems, inertial navigation, and integration.

[3] "Brief history of GPS," Aerospace Corporation, May 2023 [Online]. Available: https://aerospace.org/article/brief-history-gps

[4] "Study reveals where drivers are most reliant on their GPS," Utires.com, Feb. 2022 [Online]. Available: https://www.utires.com/articles/where-drivers-need-gps-the-most/

[5] S. Sprenger, "Over-reliance on GPS diagnosed: War game sees U.S. power challenged by spread of precision weapons," *Inside the Army*, vol. 22, no. 30, pp. 1–7, 2010. Publisher: Inside Washington Publishers [Online]. Available: https://www.jstor.org/stable/24832074

[6] L. d. A. Faria, C. A. d. M. Silvestre, and M. A. F. Correia, "GPS-dependent systems: Vulnerabilities to electromagnetic attacks," *Journal of Aerospace Technology and Management*, vol. 8, no. 4, p. 423–430, Oct 2016 [Online]. Available: https://doi.org/10.5028/jatm.v8i4.632

[7] X.-C. Zheng and H.-M. Sun, "Hijacking unmanned aerial vehicle by exploiting civil GPS vulnerabilities using software-defined radio," *Sensors and Materials*, vol. 32, no. 8, pp. 2729–2743, 2020. Tokyo Publisher: Myu, Scientific Publishing Division.

[8] A. Jafarnia-Jahromi, A. Broumandan, J. Nielsen, and G. Lachapelle, "GPS vulnerability to spoofing threats and a review of antispoofing techniques," *International Journal of Navigation and Observation*, vol. 2012, pp. 1–16, 2012. New York Publisher: Hindawi Publishing Corporation.

[9] S. Erwin. "U.S. military doubles down on GPS despite vulnerabilities." Aug. 2021 [Online]. Available: https://spacenews.com/u-s-military-doubles-down-on-gps-despite-vulnerabilities/

[10] E. Balcerak, "Briefing highlights vulnerability of gps to adverse space weather," *Space Weather*, vol. 9, no. 8, 2011. Washington Publisher: Blackwell Publishing Ltd.

[11] “Northrop Grumman Delivers 500th AN/WSN-7 Inertial Navigation System to the US Navy.” Northrop Grumman. 2022 [Online]. Available: https://news.northropgrumman.com/news/releases/northrop-grumman-delivers-500th-anwsn-7-inertial-navigation-system-to-the-us-navy

[12] “Surface Navy 2022: Next-generation navigation system on track for low-rate initial production deliveries,” Janes, Jan. 2022 [Online]. Available: https://www.janes.com/defence-news/news-detail/surface-navy-2022-next-generation-navigation-system-on-track-for-low-rate-initial-production-deliveries

[13] J. Keller. “Honeywell to replace ring laser gyros to keep Navy AN/WSN-7 shipboard navigation functioning.” Mar. 2016 [Online]. Available: https://www.militaryaerospace.com/communications/article/16714471/honeywell-to-replace-ring-laser-gyros-to-keep-navy-anwsn7-shipboard-navigation-functioning

[14] “What is Fiber-Optic Gyroscope Technology?” iXblue [Online]. Available: https://www.ixblue.com/north-america/knowledge/what-is-fiber-optic-gyroscope-technology/

[15] “Ring Laser Gyro Navigator Inertial Navigation System, AN/WSN-7(V)1,-7(V)2,-7(V)3, Part numbers CN-1695/WSN-7(V),CN-1696/WSN-7(V),and CN-1697/WSN-7(V); Operation and Maintenance, with Parts Lists,” Northrop Grumman, Mar 2003 [Online]. Available: chrome-extension://efaidnbmnnnibpcajpcglclefindmkaj/https://navytribe.files.wordpress.com/2015/11/s9427-an-omp-010.pdf

[16] M. Manicchia, “Construction and characterization of a dual atomic beam acccelerometer/gyroscope,” June 2020 [Online]. Available: https://hdl.handle.net/10945/65398

[17] D. Gervis, “Addition of a second atomic source for a dual beam atom sensor,” M.S. thesis, Monterey, CA; Naval Postgraduate School, Sep. 2021 [Online]. Available: https://calhoun.nps.edu/handle/10945/68324

[18] D. W. Keith, C. R. Ekstrom, Q. A. Turchette, and D. E. Pritchard, “An interferometer for atoms,” *Phys. Rev. Lett.*, vol. 66, no. 21, pp. 2693–2696, May 1991 [Online]. Available: https://doi.org/10.1103/PhysRevLett.66.2693

[19] M. Kasevich and S. Chu, “Atomic interferometry using stimulated Raman transitions,” *Phys. Rev. Lett.*, vol. 67, no. 2, pp. 181–184, July 1991 [Online]. Available: https://doi.org/10.1103/PhysRevLett.67.181

[20] F. Riehle, T. Kisters, A. Witte, J. Helmcke, and C. J. Bordé, “Optical Ramsey spectroscopy in a rotating frame: Sagnac effect in a matter-wave interferometer,” *Phys. Rev. Lett.*, vol. 67, no. 2, pp. 177–180, July 1991 [Online]. Available: https://doi.org/10.1103/PhysRevLett.67.177

[21] O. Carnal and J. Mlynek, “Young’s double-slit experiment with atoms: A simple atom interferometer,” *Phys. Rev. Lett.*, vol. 66, no. 21, pp. 2689–2692, May 1991. Publisher: American Physical Society [Online]. Available: https://doi.org/10.1103/PhysRevLett.66.2689

[22] S. Abend, M. Gersemann, C. Schubert, D. Schlippert, E. Rasel, M. Zimmermann, M. Efremov, A. Roura, F. Narducci, and W. Schleich, “Atom interferometry and its applications,” *Foundations of Quantum Theory*, 2019 [Online]. Available: https://hdl.handle.net/10945/64996

[23] B. Canuel, F. Leduc, D. Holleville, A. Gauguet, J. Fils, A. Virdis, A. Clairon, N. Dimarcq, C. J. Bordé, A. Landragin, and P. Bouyer, “Six-axis inertial sensor using cold-atom interferometry,” *Phys. Rev. Lett.*, vol. 97, no. 1, p. 010402, July 2006. Publisher: American Physical Society [Online]. Available: https://doi.org/10.1103/PhysRevLett.97.010402

[24] D. S. Durfee, Y. K. Shaham, and M. A. Kasevich, “Long-term stability of an area-reversible atom-interferometer Sagnac gyroscope,” *Phys. Rev. Lett.*, vol. 97, no. 24, p. 240801, Dec. 2006. Publisher: American Physical Society [Online]. Available: https://doi.org/10.1103/PhysRevLett.97.240801

[25] A. Meldrum, M. Manicchia, J. P. Davis, and F. A. Narducci, “Raman spectroscopy using a continuous beam from a 2d mot,” in *Steep Dispersion Engineering and Opto-Atomic Precision Metrology XI* (Proceedings of SPIE). Bellingham: SPIE, 2018, vol. 10548, pp. 105 481Y–105 481Y–11.

[26] M. Scully and J. Dowling, “Quantum-noise limits to matter-wave interferometry,” *Physical review. A, Atomic, Molecular, and Optical Physics*, vol. 48, no. 4, pp. 3186–3190, 1993. College Park, MD Publisher: Amer Physical Soc.

[27] T. L. Gustavson, A. Landragin, and M. A. Kasevich, “Rotation sensing with a dual atom-interferometer Sagnac gyroscope,” *Classical and Quantum Gravity*, vol. 17, no. 12, pp. 2385–2398, 2000. Publisher: IOP Publishing [Online]. Available: https://doi.org/10.1088/0264-9381/17/12/311

[28] T. Mueller, M. Gilowski, M. Zaiser, P. Berg, C. Schubert, T. Wendrich, W. Ertmer, and E. M. Rasel, “A compact dual atom interferometer gyroscope based on laser-cooled rubidium,” *The European Physical Journal. D, Atomic, Molecular, and Optical Physics*, vol. 53, no. 3, pp. 273–281, 2009.

[29] M. F. Locke and F. A. Narducci, “Navigation with atom interferometers,” Naval Air Systems Command Patuxent River United States, Rep., 2017 [Online]. Available: https://apps.dtic.mil/sti/citations/AD1041671

[30] E. Giese, W. Zeller, S. Kleinert, M. Meister, V. Tamma, A. Roura, and W. Schleich, “The interface of gravity and quantum mechanics illuminated by wigner phase space,” *Proceedings of the International School of Physics "Enrico Fermi"*, vol. 188, no. Atom Interferometry, p. 171–236, 2014 [Online]. Available: https://doi.org/10.3254/978-1-61499-448-0-171

[31] B. K. Agarwal, *X-Ray Spectroscopy: An Introduction* (Springer Series in Optical Sciences). Berlin, Heidelberg: Springer Berlin Heidelberg, 1979, vol. 15.

[32] G. Chen, D. A. Church, B.-G. Englert, C. Henkel, B. Rohwedder, M. O. Scully, and M. S. Zubairy, “Superconducting quantum computing devices,” in *Quantum Computing Devices*, vol. 6 (Chapman and Hall-CRC Applied Mathematics and Nonlinear Science Series). United Kingdom: CRC Press LLC, 2006, pp. 407–444.

[33] N. F. Ramsey, “Experiments with separated oscillatory fields and hydrogen masers,” *Science (American Association for the Advancement of Science)*, vol. 248, no. 4963, pp. 1612–1619, 1990.

[34] Y. Huang, B. Zhang, M. Zeng, Y. Hao, Z. Ma, H. Zhang, H. Guan, Z. Chen, M. Wang, and K. Gao, “Liquid-nitrogen-cooled Ca^+ optical clock with systematic uncertainty of 3×10^{-18},” *Phys. Rev. Appl.*, vol. 17, p. 034041, Mar 2022 [Online]. Available: https://doi.org/10.1103/PhysRevApplied.17.034041

[35] D. A. Steck, “Rubidium 85 D line data,” July 2021 [Online]. Available: http://steck.us/alkalidata

[36] M. Manicchia, J. Lee, G. Welch, J. Mimih, and F. Narducci, “Construction and characterization of a continuous atom beam interferometer,” 2020 [Online]. Available: https://hdl.handle.net/10945/65261

[37] D. W. Preston, “Doppler-free saturated absorption: Laser spectroscopy,” *American Journal of Physics*, vol. 64, no. 11, pp. 1432–1436, 11 1996 [Online]. Available: https://doi.org/10.1119/1.18457

[38] S. DeSavage, “The Exploration of Stimulated Raman Processes in 85 Rb Using Dual Amplitude Pulses,” M.S. thesis, University of Maryland, Baltimore County, May 2014.

[39] S. A. DeSavage, K. H. Gordon, E. M. Clifton, J. P. Davis, and F. A. Narducci, “Raman resonances in arbitrary magnetic fields,” *Journal of Modern Optics*, vol. 58,

no. 21, pp. 2028–2035, Dec. 2011 [Online]. Available: https://doi.org/10.1080/09500340.2011.606377

[40] S. A. DeSavage, J. P. Davis, and F. A. Narducci, "Controlling Raman resonances with magnetic fields," *Journal of Modern Optics*, vol. 60, no. 1, pp. 95–102, Jan. 2013 [Online]. Available: https://doi.org/10.1080/09500340.2012.761738

THIS PAGE INTENTIONALLY LEFT BLANK

Initial Distribution List

1. Defense Technical Information Center
   Ft. Belvoir, Virginia

2. Dudley Knox Library
   Naval Postgraduate School
   Monterey, California